Pantović Pavlović Marijana R., Stanojević Boris P., Pavlović Miroslav M., Mihailović Marija D., Stevanović Jasmina, Panić Vladimir V., Ignjatović Nenad, "Anodizing/Anaphoretic Electrodeposition of Nano-Calcium Phosphate/Chitosan Lactate Multifunctional Coatings on Titanium with Advanced Corrosion Resistance, Bioactivity, and Antibacterial Properties" ACS Biomaterials Science & Engineering, 7, no. 7 (2021):3088-3102, https://doi.org/10.1021/acsbiomaterials.1c00035.

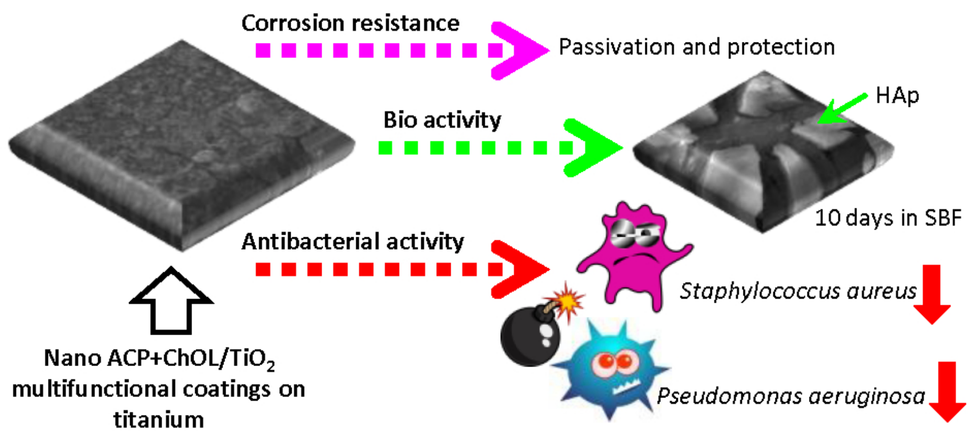

TOC Graphic

82x44mm (300 x 300 DPI)

Anodizing/anaphoretic electrodeposition of nano calcium phosphate/chitosan lactate multifunctional coatings on titanium with advanced corrosion resistance, bioactivity and antibacterial properties

Marijana R. Pantović Pavlović[a,b], *Boris P. Stanojević*[c], *Miroslav M. Pavlović*[a,b,*], *Marija D. Mihailović*[a], *Jasmina S. Stevanović*[a,b], *Vladimir V. Panić*[a,b,d], *Nenad L. Ignjatović*[e,**]

[a]Institute of Chemistry, Technology and Metallurgy, Institute of national importance for the Republic of Serbia, University of Belgrade, Belgrade, Serbia

[b]Center of Excellence in Environmental Chemistry and Engineering - ICTM, University of Belgrade, Belgrade, Serbia

[c]Faculty of International Engineering Management, Belgrade, Serbia

[d]State University of Novi Pazar, Department of Chemical-Technological Sciences, Novi Pazar, Serbia

[e]Institute of Technical Science of the Serbian Academy of Sciences and Arts, Belgrade, Serbia

ABSTRACT

The aim of this work was to investigate corrosion resistivity, bioactivity and antibacterial activity of novel nano amorphous calcium phosphate (ACP) potentially multifunctional composite coatings with and without chitosan oligosaccharide lactate (ChOL), ACP+ChOL/TiO_2 and ACP/TiO_2 ACP+ChOL/TiO_2, respectively, on titanium substrate. The coatings were obtained by new single-step *in situ* anodization of substrate to generate TiO_2 and anaphoretic electrodeposition process of ACP and ChOL. The obtained coatings were around 300±15 μm thick, and consisted of two phases, namely TiO_2 and hybrid composite phase. Both ACP/TiO_2 and ACP+ChOL/TiO_2 have improved corrosion stability, whereas the ACP+ChOL/TiO_2 coating showed better corrosion stability. It was shown that at the very start of the deposition process, formation of ChOL/TiO_2 layer takes place predominantly, which is followed by the inclusion of ChOL into ACP with simultaneous growth of TiO_2. This deposition mechanism resulted in the formation of strongly-bonded uniform stable coating with high corrosion resistance. *In vitro* bioactivity was investigated by immersion of the samples in simulated body fluid (SBF). There is in-bone-like apatite formation on both ACP/TiO_2 and ACP+ChOL/TiO_2 surfaces upon immersion into SBF, which was proven by X-ray diffraction and Fourrier Transform Infrared Spectroscopy. While ACP/TiO_2 shows no antibacterial activity, ACP+ChOL/TiO_2 samples exhibited 3 to 4- fold decreases in the number of *Staphylococcus Aureus and Pseudomonas aeruginosa* respectively, after 420 min. Probable mechanism is binding ChOL with bacterial cell wall, inhibiting its growth, altering the permeability of cell membrane and leading to bacteria death.

KEYWORDS: amorphous calcium phosphate; chitosan oligosaccharide lactate; titanium; corrosion stability; bioactivity; antibacterial activity

1. INTRODUCTION

Titanium (Ti), such as commercially pure or commercial grade 2 titanium (cp-Ti), as well as titanium alloys belong to biocompatible materials. All of them are being successfully and widely used for biomedical applications since these materials have favorable combination of properties such as: corrosion resistance, specific strength, mechanical strength, biocompatibility and chemical stability [1–9]. Titanium-based materials are considered bio-inert implantable materials since they owe chemical and biological inertness. Titanium and its alloys spontaneously form thin passive oxide films, which consist primarily of TiO_2. The spontaneous passive titanium oxide layer is stable in the physiological environment, it is predominantly amorphous and it is 2–7%nm thick [10] . Passiveness is reflected in the fact that the oxide layer behaves as a protection barrier against further surface corrosion [11,12]. However, poor osteoconductivity and osteoinductivity make titanium and its alloys not fully applicable replacement for bone tissue [13,14]. The implant surface needs to be encapsulated by a fibrous tissue without osseous junctions with the surrounding tissues in order to successful implantation occur. Unwanted body reaction upon implantation can also be caused by the presence of titanium in body [15]. Although the indigenous passive oxide film suppresses the titanium and titanium alloys corrosion with the capability to promote biocompatibility, the major disadvantage of titanium surfaces pertains to their continuous de-passivation and re-passivation under mechanical stress in body fluids [10]. These two competing processes can lead to incorporation of different alloy elements and surrounding solutions into the passive film [16,17]. These alloying elements and impurities are most certainly not involved to significant content, but dissolution of alloying elements and incorporation of different elements from surrounding solutions into the passive film during time that the implant is present in the body is possible. These effects may well play a role in orthopaedic implants as re-passivation at the osseous implantation site is able to lead to the adsorption of calcium and phosphate ions into the passive film.

Taking into account these considerations, there is a requirement for suitable surface modification of titanium and its alloys that will result in improved biocompatibility and osteointegration, with simultaneous reduction of strong bacterial seeding on the implant surface [16,18–22]. Generally, titanium implants are treated with bioactive materials, in most cases bioactive ceramic materials, in order to improve implants biocompatibility and osteointegration [22–25].

Biomedically-relevant and bioactive calcium phosphates are represented by amorphous calcium orthophosphates (ACPs). ACPs are known upon adjustable chemical properties, but, on another hand, ACPs have practically identical glass-like physical properties with neither orientational nor translational long-range orders of the atomic positions [26]. Calcium phosphates (CPs), and among them synthetic hydroxyapatite (HAp, $Ca_{10}(PO_4)_6(OH)_2$), have found its predominant use in bone tissue engineering as a result of their exeptional biocompatibility. Synthetic HAp coatings are considered to improve bioactive and osteoconductive properties of biomaterial surfaces because of high biocompatibility and chemical composition much like the natural CP-based bone tissue [27].

ACPs tend to be formed as a precursor phases in supersaturated solutions with stable pH [24]. ACPs are easily transformed to thermodynamically stable hydroxyapatite under these conditions. Various additives and process parameters may influence the stability of ACPs and their transformation to crystalline HAp phases [28].

Nonetheless, as the result of poor mechanical properties of CP-based biomaterials, the development of composite coatings combining various CPs with biopolymers is gaining increasing interest. Chitosan-based CP coatings have been suggested for bone tissue engineering [29–32] with enhanced corrosion resistance. Electrodeposited HAp nanocomposite coatings with sodium alginate with tailored morphology and microstructure were fabricated, where the obtained results might be very helpful in the further development of alginate-based composite coatings for biomedical engineering. The later statement is especially true for bioactive coatings for bone implants [33]. Additionally, it was shown that chitosan oligosaccharide lactate (ChOL)-coated HAp novel composite coatings have promising properties that can improve the delivery of steroid drugs while it targets the breast cancer cells [27]. ACP has been suggested to protect the proteins from thermal denaturation [34]. CP coatings containing chitosan and heparin showed improved blood compatibility [30] and some chitosan multilayered coatings were used as multifunctional implants [32].

It can be found in the literature that chitosan was deposited by galvanic coupling on stainless steel, where the coating showed improved corrosion stability and satisfying biocompatibility [35] The literature reports that some synthetized Chitosan/HAp coatings on Ti substrate can be produced cataphoretically [31]. However, this was managed in somewhat complicated, two-step process. CPs were demonstrated to be good candidate for protein protection [34], while investigations of chitosan oligosaccharide lactate ceramic composites for drug delivery have suggested the advanced properties of this product in comparison to chitosan itself [27].

Electrophoretic deposition technique (EPD) is cost- and time-effective method which generates a coating of bioceramic particles at the surface of implant material. The deposition is driven by an electric field imposed to the precursors' suspension, when an electric field is applied between two conductive electrodes [4,12,29,36–38]. The factors impacting the EPD coating quality are the deposition period, the applied voltage, the suspension composition and concentration. EPD provides simple control of the thickness and morphology of deposited coating through basic adjustment of the deposition period and applied voltage [39,40].

In developing the materials for biomedical application, one of the most challenging requirements is corrosion resistance [41]. When implants' corrosion is considered, the pitting and galvanic corrosion are common processes for dental implants, while pitting and fretting corrosion, as well as corrosion fatigue, are principal corrosion processes that occur on orthopaedic implants [1,41]. The implant corrosion is usually defined as slow degradation of the implant due to electrochemical reaction between the implant surface and electrolyte. On the other hand, implants are also subjected to mechanical loads and changes in pH, both of which can intensify the corrosion process and lead to higher corrosion damage. Usual act to enhance corrosion resistance of titanium implants is to increase the oxide layer surface thickness by applying an electrochemical anodization process. However, to authors' knowledge there is no literature data on corrosion resistance of composite ACP/TiO_2 and ACP+ChOL/TiO_2 coatings on titanium.

This particular research reports corrosion resistance, bioactivity and antibacterial properties of composite ACP/TiO_2 and ACP+ChOL/TiO_2 coatings on titanium obtained by single-step *in situ* anodization/anaphoretic electrodeposition for potential biomedical application.

2. MATERIALS AND METHODS

2.1. Preparation of suspensions and samples for coating deposition

An aqueous calcium nitrate ($Ca(NO_3)_2$) solution (150 mL; 26.6 wt%) was added dropwise to the solution of ammonium phosphate (having following composition: 7 mL H_3PO_4 + 165 mL NH_4OH + 228 mL H_2O) at 50 ˚C during 60 min, while being magnetically stirred at 100 rpm. The obtained gel was additionally washed three times with distilled water. Solid phase was extracted by centrifugation at 4000 rpm and 5 ˚C for 1 h. The resulting precipitate was immediately freeze-dried (Freeze Dryer Christ Alpha 1-2/ LD Plus) at -30 ˚C and 0.37 bar for 1 h. The final freeze-drying of the obtained powder was carried out at -40 ˚C and 0.12 bar for 2 h. All used chemicals are obtained from Sigma-Aldrich, Germany.

For *in situ* anaphoretic deposition of composite coatings, absolute ethanol suspensions of dried ACP powder were prepared. Total volume%of%each prepared suspension were 120%mL each. Depending on the sample, suspensions contained: 1 mass % of nanosized ACP [24] for ACP/TiO_2 composite coating deposition, and 1 mass % of nanosized ACP and 0.05 mass % of ChOL (Sigma, average Mn 5,000) for ACP+ChOL/TiO_2 composite coating deposition. 10%mass% of NaOH was added to each suspension in order to achieve pH value of 10. The suspensions were ultrasonicated in Sonicor S-101 ultrasonic bath with US frequency of 40 kHz for 15%min to reach uniform and ample stable state for the duration of EPD process. The titanium plates (dimensions: 20 mm × 10 mm × 0.89 mm, for surface analysis, Sigma - Aldrich, 99.7 % purity) were used as substrates for anaphoretic deposition of composite coatings. Before deposition, Ti plates were abraded with silicon carbide (SiC) paper of successive grades from 600 to 2000 grit and further mechanically polished with alumina pastes of 1, 0.3 and 0.05 μm, successively. All of the Ti substrates were ultrasonically cleaned in ethanol solution for 15 min.

A two-electrode EPD cell arrangement was used for *in situ* anaphoretic electrodeposition. The anode was a titanium plate, whereas 316L stainless steel plates positioned on both sides of the anode, leaving a cathode/anode gap of 10 mm from the anode, were used as cathodes. The applied anodizing voltage was 60 V, since previous research has shown that rougher surface with greater root-mean sqare roughness (RMS) is obtained at lower voltages [4,12,24]. The EPD cell was filled with a suspension and purged with N_2 for 30 min. An Aim and Thurlby Thandar Instruments TTi CPX400DP Bench/System/ATE Programmable DC power supply was used as power supply. Prior to anaphoretic depositions, all the suspensions were ultrasonically treated for additional 30 min to obtain uniform particle distribution. The suspensions were continuously stirred by magnetic stirrer during anaphoretic deposition. The ACP/TiO_2 and ACP+ChOL/TiO_2 composite coatings on Ti were obtained at constant voltage regime for a deposition time of 3 min, at 25 ˚C. Coatings were rinsed with distilled water and air dried at room temperature.

2.2.Characterization of the samples

The surface physical appearance of deposited coatings was analyzed by field-emission scanning electron microscopy (Tescan Mira 3 XMU FEG-SEM). EDS analysis was performed on a Jeol JSM 5800 SEM with SiLi X-ray detector (Oxford Link Isis series 300, UK), connected to the SEM and a multi-channel analyzer. Fourier transform infrared spectroscopy (FTIR) was carried out using Michelson MB Series Bomen FTIR spectroscope (Hartmann Braun) to detect the bond types in the material. The scan was carried out in the wavenumber range of 500–4000 cm^{-1} with a resolution of 0.5 cm^{-1}. Structural and phase evaluation of the composite samples have been performed by X-ray diffraction (XRD) measurements on Philips PW 1050 powder diffractometer at room temperature with Ni-filtered CuKα radiation (λ%=%1.54178%Å) and scintillation detector within 2θ range of 10–82˚ in steps of 0.05˚. The scanning rate was 5%s per step. Phase analyses were performed using EVA V.9.0 software.

2.3. Mineralization in SBF

In vitro bioactivity evaluation was conducted by adapting the protocol formulated by the Kokubo [42–44] to assess the apatite-forming ability of the composite coatings. Bioactivity was assessed by vertically soaking the coated specimen in a plastic vial containing 40 mL of simulated body fluid (SBF) solution maintained at 37 ˚C for 240 h. The composition of the SBF solution, which contained reagent-grade salts (all from Sigma-Aldrich) dissolved in deionized water (142.0 mM Na^+, 5.0 mM K^+, 1.5 mM Mg^{2+}, 2.5 mM Ca^{2+}, 4.2 mM HCO_3^-, 147.8 mM Cl^-, 1.0 mM HPO_4^{2-} and 0.5 mM SO_4^{2-}), was similar to human blood plasma. The final solution was buffered by tris(hydroxymethyl)aminomethan and pH adjusted to 7.40 with 1 M hydrochloric acid. The SBF was replenished daily to maintain the concentration of the ions. Each of the samples was gently washed with deionized water and dried at 37 ˚C before characterization by SEM and XRD analyses.

2.4. Electrochemical measurements

Electrochemical measurements had been conducted in SBF at 37 ˚C. A standard three-electrode arrangement was used to perform electrochemical potentiodynamic and impedance spectroscopy measurements. The working electrodes were testing samples (Ti plate, ACP/TiO_2 and ACP+ChOL/TiO_2 composite coatings on Ti), the counter electrode was a platinum mesh, while the reference electrode was saturated calomel electrode (SCE). The testing surface area was 1 cm^2. All measured and mentioned potentials within the paper are referred to SCE. All of the electrochemical measurements have been executed with a Reference 600TM potentiostat/galvanostat/ZRA (Gamry Instruments Inc., Warminister, PA, USA). Impedance data were collected at the open-circuit potential (OCP) over a broad frequency range (100 kHz–10 mHz) using 10 mV rms amplitude of sinusoidal input voltage. Impedance spectra were analyzed and fitted by ZView® software [45,46]. Potentiodynamic measurements were carried out from a cathodic potential of −250 mV to an anodic potential of 250 mV with respect to E_{OCP} and from -1 V cathodic potential to 4 V anodic potential with respect to $E_{OCP.}$ Scan rate was 1 mV/s. E_{OCP} measurements were carried out for 2400 s (40 min) and the results were recorded every 0.5 s or ±0.001 mV change of E_{OCP}.

2.5. Antibacterial activity assay

The antibacterial activity of pure, untreated titanium substrate, ACP/TiO_2 and ACP+ChOL/TiO_2 composite coatings was examined against the Gram-positive pathogenic bacterium strain *Staphylococcus aureus,* ATCC 25923, and Gram-negative bacterium strain *Pseudomonas aeruginosa* PAO1, ATCC 15692, in Mueller Hinton Broth (MHB) suspension using a spread-plate method. Bacterial strain colonies (*P. aeruginosa PAO1* and *S. aureus*) were tempered at 37 ˚C and left overnight without aeration to develop an overnight bacterial culture. The optical density of the overnight culture at 600 nm was assessed and then adjusted to 0.4 by dilution with MHB medium to reach 10^8 bacteria per mL. These overnight cultures were further diluted. Serial dilutions of samples were mixed with melted Luria-Bertani LB agar and poured into Petri dishes. Aliquots were taken at the beginning of the experiment and consecutively every hour for 7 h of incubation. Control groups for both bacterial strains consisted only of overnight bacterial cultures in MHB. A spectrophotometer was used to establish the growth curve, by measuring the optical density of bacteria. The experiments were performed in triplicate in three independent measurements.

Bacteria from the measurements after 420 min of incubation were seeded on sterile solid Mueller Hinton Agar (MHA) nutrient media to determine the number of bacterial cells at the end of the experiment. 100 μl from an Erlenmeyer flask was inoculated and diluted to obtain a countable number of colonies on a petri dish and rubbed with a sterile glass rod. Dilutions were made using 0.01 M $MgSO_4$. Petri dishes were incubated for 16 h at 37 °C, after which the number of grown colonies was counted. The control groups were obtained after seeding bacteria strains from the first set of experiments control groups after 420 min on MHA. As previously explained, the experiments were performed in triplicate in three independent measurements. All used chemicals are from Sigma-Aldrich, Germany.

In order to test antimicrobial properties, the anti-biofilm efficiency of ACP/TiO_2 and ACP+ChOL/TiO_2 composite coatings was examined by the evaluation of viable cell count (VCC) and bacterial culture density measurements. VCC measurements were carried out at the end of the experiment, *i.e.*, after 420 min has passed. Taking into consideration structural differences of the bacterial cell wall, *Staphylococcus aureus* and *Pseudomonas aeruginosa* PAO1 were investigated after period of 420 minutes.

3. RESULTS AND DISCUSSION

3.1. FTIR studies

Figure 1 displays the FTIR spectra of synthesized ACP/TiO_2 and ACP+ChOL/TiO_2 coatings, in which the characteristic absorption bands at corresponding wave numbers are stated. Figure 1 proves the successfulness of the *in situ* process of simultaneous anodization of Ti substrate and electrophoretic deposition of both ACP and ACP+ChOL coatings.

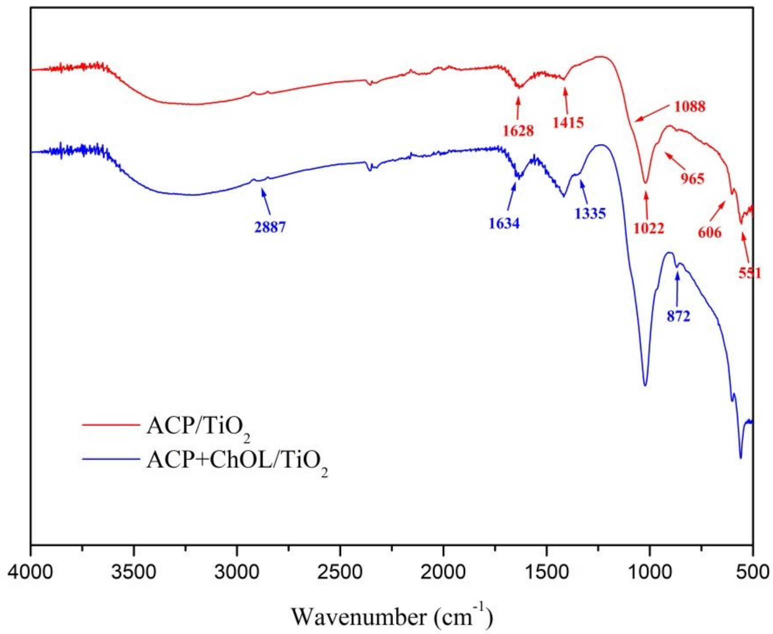

Figure 1. FTIR spectra of ACP/TiO_2 and $ACP+ChOL/TiO_2$ composite coatings on titanium substrate.

FTIR spectrum of ACP/TiO_2 composite coating displays common PO_4^{3-} distinctive absorption bands of ACP. The characteristic bands at 551 and 606 cm^{-1} are attributed to the P–O bond within the phosphate group (the ν4 vibrational mode) [47]. The most distinguished adsorption band is the adsorption peak at 1022 cm^{-1} which belongs to ν3 phosphate mode region, with the two apparent shoulders at 1088 and 965 %cm^{-1} which should be linked to ν1 and ν3 phosphate modes [48]. The presence of weak peak at 1415%cm^{-1} is attributed to C=O. It is assigned to the carbonate (CO_3^{2-})

group in ACP, and it corresponds to the ν3 asymmetrical stretching vibration of the CO_3^{2-} group [47,49]. The positions of the carbonate bands suggest partial substitution of hydroxyl groups by carbonate groups in ACP. FTIR is very sensitive method to these carbonate substitutions and even a tiny quantity of carbonate can be detected accordingly[24,48].. The weak absorption band at 1628%cm^{-1} is from bending modes of absorbed water [24,48].

Besides mentioned absorption bands that could be related to ACP, the ACP+ChOL/TiO_2 coating exhibits a peak at 872 cm^{-1} from the deformation of the β-glycosidic linkage [50], affiliated to the –C–O–C group vibration assigned to the saccharide structure [51,52]. The peak at 1335 cm^{-1} is assigned to the so-called amide III band and is caused by linked C–H/N–H deformation vibrations [53]. The band at 1634 cm^{-1}, which overlaps with weak absorption band at 1628%cm^{-1} from the absorbed water, is assigned to the amide I band (stretching vibration of the C=O group from R–C(=O)NR'R"). The characteristic weak band at around 2887 cm^{-1} is attributed to –CH backbone vibrations [24,50,51,53–55]. All of these identified bands are characteristic for chitosan oligosaccharide lactate.

3.2. Potentiodynamic polarization studies

Figure 2 shows the open circuit potential curves prior to the polarization and potentiostatic electrochemical impedance spectroscopy (PEIS) measurements. In order to achieve a stable E_{OCP} reading, the samples were immersed in the simulated body fluid solution for 2400 s, while their E_{OCP} was recorded throughout.

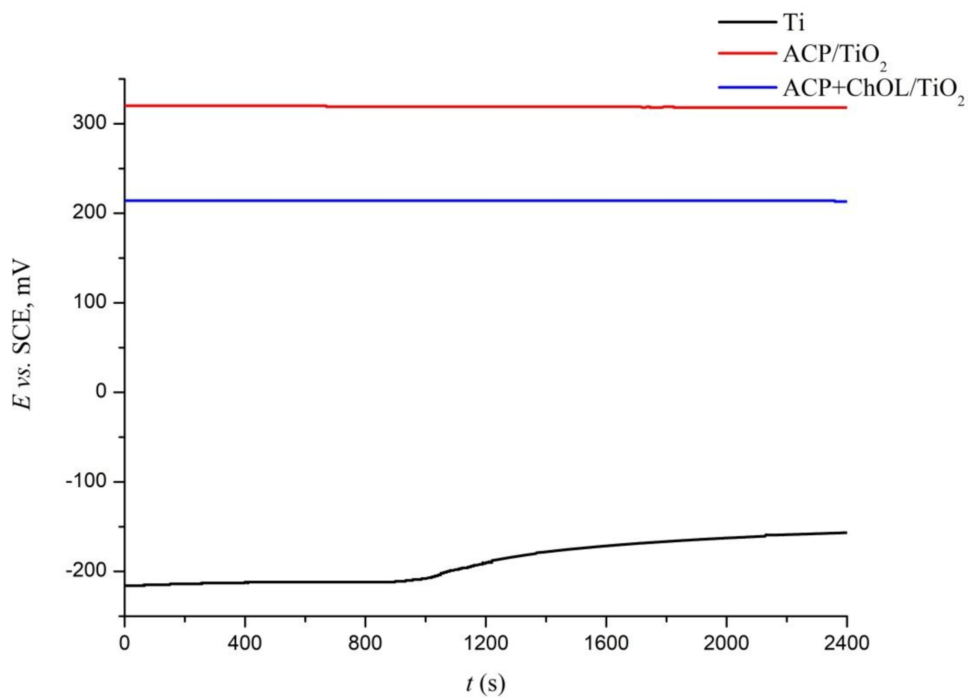

Figure 2. Results of OCP measurements of bare Ti, ACP/TiO_2 and $ACP+ChOL/TiO_2$ composite coatings on titanium during 2400s.

It can be seen that both ACP/TiO_2 and $ACP+ChOL/TiO_2$ have positive, steady and constant open circuit potentials. On the other hand, pure grade 2 titanium which was treated prior to experiments, as explained in the experimental section, shows E_{OCP} that gradually shifts to positive direction. The potentials of *in situ* anodized/anaphoreticaly deposited ACP/TiO_2 and ACP+ChOL/TiO_2 composite coatings on titanium are, hence, nobler than those of the cp-Ti, which signals better surface passivation and protection[1,56]. E_{OCP} of pure cp-Ti starts off at -216 mV and shifts towards the passive direction, building up passive protective oxide film [57]. At the end of measurement the OCP slope decreased gradually with time and stabilized, finally. This manifestation shows that formed passive film reached the dynamic balance between the film's formation and dissolution [57–59].

The potentiodynamic polarization curves of pure, uncoated cp-Ti, ACP/TiO_2 and ACP+ChOL/TiO_2 composite coatings on titanium in SBF solution having pH 7.4 are presented in Figure 3. Their corrosion properties could be appraised using the corrosion current density, j_{corr}. The corrosion potential (E_{corr}), corrosion current density (j_{corr}), anodic/cathodic slopes (β_a and β_c) and polarization resistance (R_P) values are derived from the polarization curves using Tafel extrapolation method.

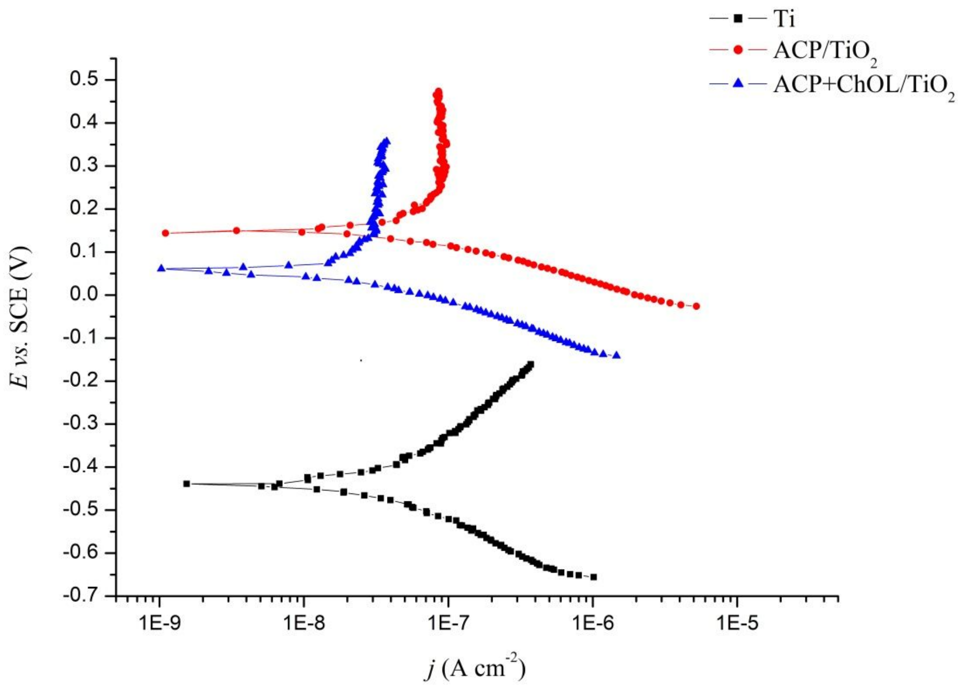

Figure 3. The potentiodynamic polarization curves of bare Ti, ACP/TiO_2 and $ACP+ChOL/TiO_2$ composite coatings on titanium measured from a cathodic potential of −250 mV to an anodic potential of +250 mV in SBF

Polarization resistance was calculated by Stern-Geary Equation (1):

$$R_P = \frac{B}{j_{corr}} = \frac{\Delta E}{\Delta j_{\Delta E \to 0}} \quad (1)$$

where B is determined empirically from the cathodic and anodic slopes of Tafel plots (Equation 2)

$$B = \frac{\beta_a \beta_c}{2.3(\beta_a + \beta_c)} \qquad (2)$$

The protective efficiencies (*PE*) of the composite coatings were calculated using the Equation (3) [60]:

$$PE(\%) = \frac{R_P(\text{coating}) - R_P(uncoated)}{R_P(coating)} \times 100 \qquad (3)$$

where, R_P(coating) and R_P(uncoated) are the polarization resistances of the composite coatings on titanium and uncoated cp-Ti, respectively. The total porosity (*P*) of the composite coating was evaluated using the Elsener's empirical equation (Equation 4) [61]:

$$P = \frac{R_P^0}{R_P} \times 10^{-\left(\left|\frac{\Delta E_{corr}}{\beta_a}\right|\right)} \qquad (4)$$

where R_P^0 and R_P are the polarization resistances of the uncoated and composite coated Ti, respectively, ΔE_{corr} is the difference between corrosion potentials of the uncoated and composite coated Ti. These values are put together in Table 1.

Table 1. Electrochemical parameters from potentiodynamic polarization measurements of bare Ti, ACP/TiO_2 and ACP+ChOL/TiO_2 composite coatings on titanium

Sample	**Ti**	**ACP/TiO_2**	**ACP+ChOL/TiO_2**
E_{corr} **(mV vs SCE)**	-440	149	77
j_{corr} **(nA cm^{-2})**	42	30	15
β_a **(mV dec^{-1})**	277	193	178
β_c **(mV dec^{-1})**	-163	-145	-115
PE **(%)**	–	11	46
P **(%)**	–	0.66	0.74
E_b **(mV vs E_{OCP})**	196	982	859

It may be seen from curves shown in Figure 3 as well as the results in Table 1 that corrosion current density values are lower for the ACP/TiO_2 and ACP+ChOL/TiO_2 composite coatings on titanium in SBF solution when compared to those for the cp-Ti. The creation of ACP and ChOL multifunctional composite coating on Ti surface substantially improved its corrosion resistance. Better corrosion stability was achieved by inclusion of 5 wt.% of ChOL to the starting anodizing solution compared to pure ACP soultion. The corrosion potential shifts to positive direction and j_{corr} decreases in the presence of composite coatings. These findings are consistent with the results of OCP measurements. ACP+ChOL/TiO_2 composite coating showed the lowest j_{corr} value (15.38%×%10^{-9}%A%cm^{-2}), that had been approximately three times lower compared to the corrosion current density value for pure cp-Ti sample, while ACP/TiO_2 composite coating exhibited j_{corr} value which had been 50% lower compared to the pure cp-Ti sample (29.99%×%10^{-9}%A%cm^{-2}). Better corrosion stability of both ACP/TiO_2 and ACP+ChOL/TiO_2 samples suggests that the corrosion behavior and endurance of the samples in the SBF medium was highly affected by the formation of both inhomogeneous and homogeneous oxides, as well as ceramic and composite layers. Owing to high molecular size and molecular weight of ChOL, the surface coverage of the Ti metal is large [62]. The inclusion of ChOL in ACP with simultaneous titanium oxide formation, which was proven and explained in previous work [24] most likely helps in the formation of well bonded consistent stable coating on titanium surface. Hence the corrosion stability of both ACP/TiO_2 and ACP+ChOL/TiO_2 composite coatings can be attributed to the barrier layer formed on Ti metal which inhibits the direct contact of metal surface with the SBF solution.

Polarization diagrams over a broader potential range are shown in Figure 4. Besides already mentioned parameters, such as E_{corr}, j_{corr}, β_a, β_c and R_P, the breakdown potential (E_b) of the passive film can be resolved. E_b can be determined at the inflection point or at an arbitrary current density value above the sharp change in slope. The E_b values are also shown in Table 1.

A stable passive behavior for each of the samples can be observed from Figure 4. E_b values show that this passive behavior occurs up to 0.859 V for ACP+ChOL/TiO_2 and up to 0.982 V for ACP/TiO_2 samples. These values are significantly higher than the expected existing redox conditions in human body [53]. In composite coatings, one can find positive shifts of E_b in comparison to uncoated cp-Ti substrate, as a result of more compact passivation.

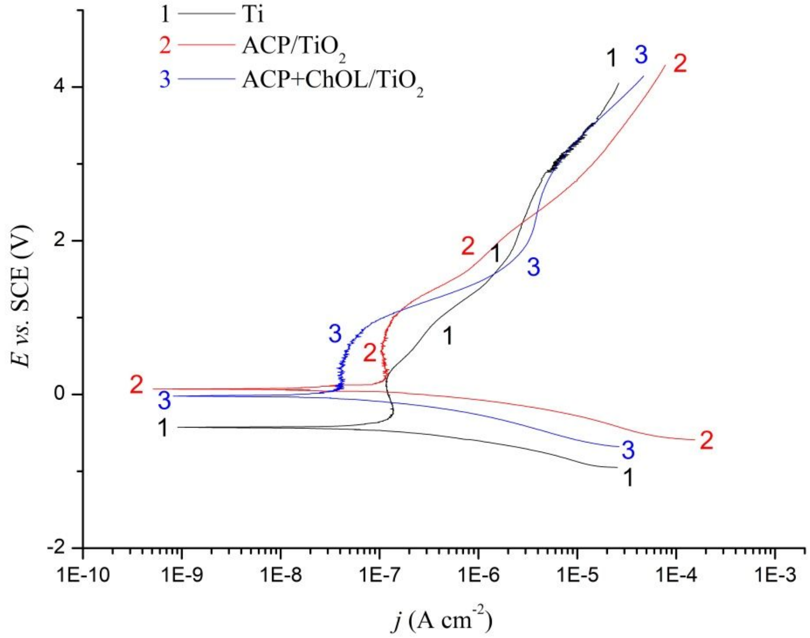

Figure 4. The potentiodynamic polarization curves of bare Ti, ACP/TiO_2 and ACP+ChOL/TiO_2 composite coatings on titanium measured from a cathodic potential of −1 V to an anodic potential of +4 V in SBF

It has been found that high corrosion resistance of material is reflected in R_P values of 10^6%Ω%cm^2 and higher [63]. The obtained results suggest that both ACP/TiO_2 and ACP+ChOL/TiO_2 coated composites showed higher R_P values than pure cp-Ti, although the cp-Ti itself has the R_P value of 10^6%Ω%cm^2. The increased corrosion resistance for ACP/TiO_2 and ACP+ChOL/TiO_2 coated composites compared to cp-Ti sample is due to the development of barrier layer towards assertive ions from the electrolyte. The ACP/TiO_2 and ACP+ChOL/TiO_2 coatings help to protect metal substrate from the attack of anions, but, additionally, ChOL composite film incorporates ACP structure, and it is able to act also as a barrier layer around the Ti implant surface. This can be observed from the porosity values, where the considerable reduction in the corrosion rate can be correlated to the decrease in porosity in composite coating (0.66% for ACP/TiO_2 and 0.74% for ACP+ChOL/TiO_2 coatings). The low porosity clearly indicates the compact morphology of composite coatings. High R_P values and low porosity values show relatively higher protection efficiency when compared to the pure Ti. It has been found that *in situ* anodization/anaphoretic deposition increases the adhesion strength of the ACP+ChOL/TiO_2 com-posite coating [24], and the potentiodynamic polarization studies show increased corrosion resistance of the sample. During the *in situ* anodization/anaphoretic deposition two competing processes take place. Anodization of Ti leads to evolution of O_2, which forms tubular-like shapes on the surface. This evolution of O_2 is locally changing pH value at the vicinity of the substrate, and two phases are formed. This local change of pH value damages negatively charged micelle of ACP and ChOL powders and deposition of these powders onto the surface occurs. Since this process happen almost instantaneously and simultaneously the adhesion is improved. The nobler

E_{corr} and lower j_{corr} values indicate the ability of ACP/TiO_2 and ACP+ChOL/TiO_2 composite coated samples to offer a better corrosion resistance for Ti (Figures 3 and 4 and Table 1).

Another specific feature can be observed from Figure 4. There are two obviously distinguishable passive areas in cp-Ti and ACP+ChOL/TiO_2 samples, and this specific aspect is not clearly seen in ACP/TiO_2 sample. From the electrochemical point of perspective, ChOL emphasizes pure cp-Ti behavior, but in nobler direction, and with increased corrosion stability. ACP+ChOL/TiO_2 sample clearly shows two-step passivation. The initial passive region covers a broad potential range, and it occurs as the result of effective blocking of the materials surface by the coating layer [64], while steady second passivation occurs due to the creation of a compact passive layer at the substrate/coating interface.

3.3. Potentiostatic electrochemical impedance spectroscopy studies

On the foundation of obtained results from Tafel studies, PEIS was utilized to assess the corrosion behavior of the ACP/TiO_2 and ACP+ChOL/TiO_2 composites coated over Ti in SBF solution and are reported in the form of complex plane plots in Figure 5. PEIS was recorder at E_{OCP} for both samples.

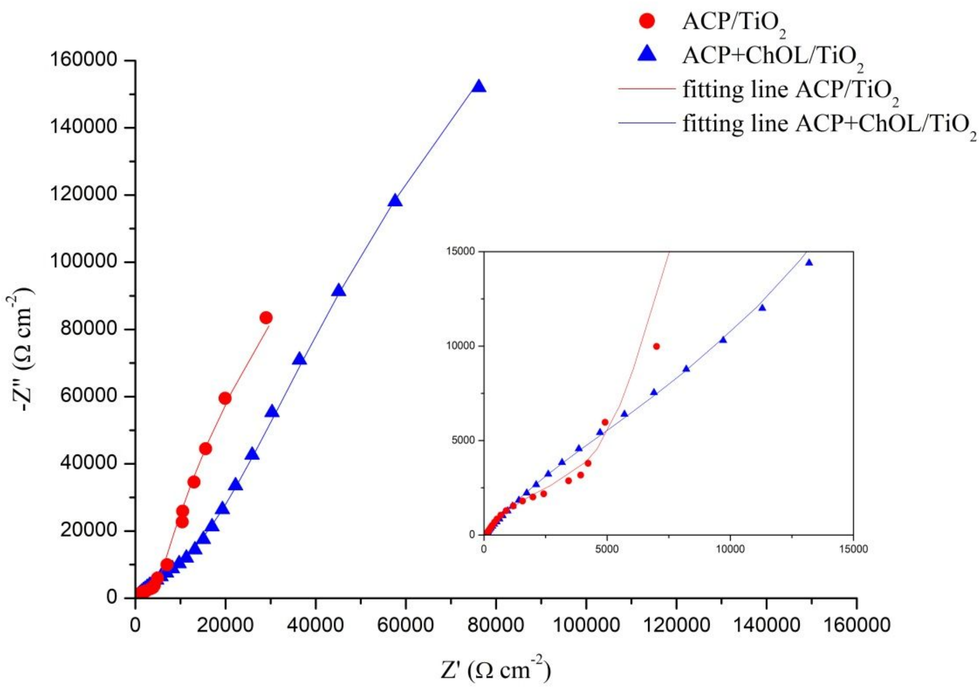

Figure 5. The complex plane plots of ACP/TiO_2 and ACP+ChOL/TiO_2 composite coatings on titanium.

The coated samples exhibited an impedance loops at high frequencies of large diameters. Based on the PEIS data, Figure 6 shows equivalent electrical circuit (EEC) models used to fit the data from Figure 5. The impedance spectra were fitted with an EEC consisted of the following elements Rs (CPEdlRct) (CPEcRc) for the ACP/TiO_2 coated sample (Figure 6a), where Rs, Rc, CPEc, Rct, and CPEdl are the resistance of the solution, the resistance of the coating, the capacitance of the coating, corrosion-related charge transfer resistance and the capacitance of the double layer, respectively. The Rs (CPEdlRct(CPEpRp)) (CcRc) model was used to fit the data of ACP+ChOL/TiO_2 coating on Ti (Figure 6b), where Rp and CPEp are the diffusive resistance in pores and the capacitance of the pores, respectively.

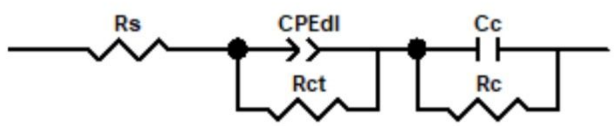

a)

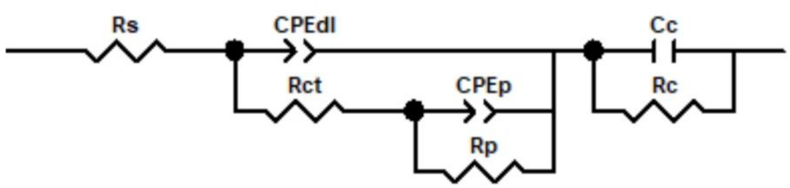

b)

Figure 6. The equivalent electrical circuits used to fit the impedance spectra of: a) ACP/TiO_2 and b) ACP+ChOL/TiO_2 composite coatings.

The PEIS data have been effectively fitted by EECs shown in Figure 6. The χ^2 values of all fittings provided (the lines in complex plane plots, Figure 5) was below 5×10^{-4}, with a data-modulus type of data weighting through 100 iterations. For ACP/TiO_2 composite coating, the time constant at high frequencies (RctCPEdl) is related to the outer porous layer, while the time constant at low frequencies (RcCPEc) corresponds to great corrosion behavior and stability of the inner barrier layer [65]. The same stands for ACP+ChOL/TiO_2 coating, whereas for this sample diffusion of the SBF through pores can be noted, and the time constant at low frequencies corresponds to (RcCc), since it behaves as real capacitor. The constant phase element, CPE, is used in EEC instead of a capacitor, C, in order to better embrace the non-ideal behavior of the C element, namely to address the surface heterogeneities, surface roughness, as well as defects on the surface. In general, the following Equation 5 is used as definition of the impedance of CPE:

$$Z_{CPE}=[Y(j\omega)^n]^{-1} \quad (5)$$

where Y is the frequency-independent real constant of the CPE, ω being the angular frequency ($\omega=2\pi f$) in rad s^{-1}, f is the frequency, n is the value of the exponent of CPE between −1 for an ideal inductor and 1 for an ideal capacitor.

Obtained results for examined materials from fitting results using EEC are given in Table 2.

Table 2. Electrochemical impedance spectroscopy data for ACP/TiO_2 and ACP+ChOL/TiO_2 composite coatings on titanium substrates.

Sample	**ACP/TiO_2**	**ACP+ChOL/TiO_2**

R_s (Ω cm^2)	63.85	46.94
R_{ct} (Ω cm^2)	5223	16700
Y_{dl} (s^n Ω^{-1} cm^{-2})	3.48×10^{-5}	1.86×10^{-5}
n	0.71	0.67
C_{dl} (F cm^{-2})	1.73×10^{-5}	7.15×10^{-6}
R_p (Ω cm^2)	-	32691
Y_p (s^n Ω^{-1} cm^{-2})	-	2.73×10^{-5}
n	-	0.5
C_p (F cm^{-2})	-	2.44×10^{-5}
R_c (Ω cm^2)	9.02×10^5	1.22×10^6
Y_c (s^n Ω^{-1} cm^{-2})	1.03×10^{-4}	-
n	0.90	-
C_c (F cm^{-2})	1.62×10^{-4}	9.51×10^{-5}

The structural similarity of the impedance spectra of both Ti-based biomaterials is obvious, as a result of fact that the electrochemical response of the biomaterials is dependent on their similar protective layer on their surface. Nevertheless, it is possible to observe some differences.

From the obtained PEIS results for both ACP/TiO_2 and ACP+ChOL/TiO_2 composite coatings, it can be seen that ACP+ChOL/TiO_2 has more uniform inner passive layer/film, with real capacitive response (n_{dl} is 0.90 for ACP/TiO_2, and real capacitive behavior for ACP+ChOL/TiO_2). This intrinsic layer appears a lot more defined with ACP+ChOL/TiO_2 than at ACP/TiO_2 composite coating. Thus, it substantially contributed to the protective ability of the coating as a whole. Two-step passivation and protection can be seen in both coatings (Figure 4), while with ACP+ChOL/TiO_2 composite coating the presence of wider pores is evident from the heterogeneous character of the outer layer (presence of CPEp and Rp). These pores can be observed on Figure 7b.

At the very beginning of the *in situ* anodization/anaphoretic deposition process, there is formation primary of titanium oxide layer, followed by ChOL, since ChOL is more affected by applied EPD field due to greater polarity of ChOL comparing to ACP. There is simultaneous anodization of Ti substrate, and deposition of ChOL, and afterwards ChOL/ACP. PEIS results suggest that there is formation of pores within the outer layer; these pores are larger than in ACP/TiO_2 samples, and the diffusion of SBF through pores is prone to occur. Hence, finite diffusion limitations through the pores anticipate the overall corrosion resistance of the ACP+ChOL/TiO_2 composite coating. Once the pores appeared, the presence of ChOL in these pores is evident, and the response of the coating reflects it's more compact and homogenous structure.

As per the above mentioned considerations, it seems that the homogeneous passive protective contribution of the ACP+ChOL/TiO_2 coating is embroiled much in those EEC elements related to the inner surface of the coating. The components relating with the outer surface, which directly faces the bulk of solution, are mainly governed by the pore resistance and double layer charging/discharging processes. It is to be assumed that corrosion processes are localized around bottoms of the pores/cracks of a layer. This is more evident if one can multiply the charge transfer resistance with the actual available surface for corrosion. In the other words, the ratio of R_{ct} of ACP/TiO_2 and ACP+ChOL/TiO_2 coatings is 0.32, which means that there is only 32% of surface available for corrosion in ACP+ChOL/TiO_2 samples with respect to that surface of ACP/TiO_2. It can be also roughly estimated by comparing the areas around the cracks in Figure 7b, enlarged part, where the surface of the pores/cracks is close to *ca.* 1/3 of the scanned surface. The realistic assumption is that available surface at the bottom of the furrow is twice the size of the visible furrow surface, hence the area of the furrows is roughly one third of the size of the whole coating area.

By applying the potential difference between cathode and anode (working titanium electrode) there is instantaneous formation of TiO_2 passive layer, as the fastest occurring reaction, since it is the only reaction that is not diffusion controlled. Only then the simultaneous anodization of the substrate (which leads to TiO_2 formation) with anaphoretic deposition of ChOL and ACP occurs. PEIS suggests that deposition favors ChOL deposition on formed TiO_2 layer over ACP, with gradual decrease in ChOL concentration and gradual increase in ACP concentration of the coating, while there is still formation of new TiO_2 that incorporates into the coating. This *in situ* process of coating formation leads to improved adhesion [24] and corrosion resistance.

As already mentioned, the higher the coating resistance and the coating capacitance, the more resistive is the sample to the corrosion. The PEIS results are, hence, in good agreement with the results obtained from potentiodynamic polarization studies.

3.4. Coatings morphologies and immersion studies

Ability to create an apatite layer when the substrate is in contact with biological (or biological alike) fluids is referred to as *in vitro* bioactivity of the substrate. Moreover, the ACP/TiO_2 and ACP+ChOL/TiO_2 composites on Ti substrates form a bone-like apatite layer (later proven by XRD measurements) on their surfaces upon immersion in SBF solution. Therefore, in order to assess the biocompatibility of the composite coatings, ACP/TiO_2 and ACP+ChOL/TiO_2 composites on Ti substrates were immersed in SBF solution and analyzed at various time periods. SEM was accustomed to characterize the surface area physical appearance and size of constituting particles of synthesized ACP/TiO2 and ACP+ChOL/TiO2 composite coatings on titanium substrates, as well as morphologies of the surfaces after immersion in SBF solution for different periods.. Morphology of the ACP/TiO_2 and ACP+ChOL/TiO_2 composites surfaces before immersion in SBF solution are shown in Figure 7a and b, while the morphologies of the coatings immersed in SBF solution at various time periods are shown in Figure 7c-f.

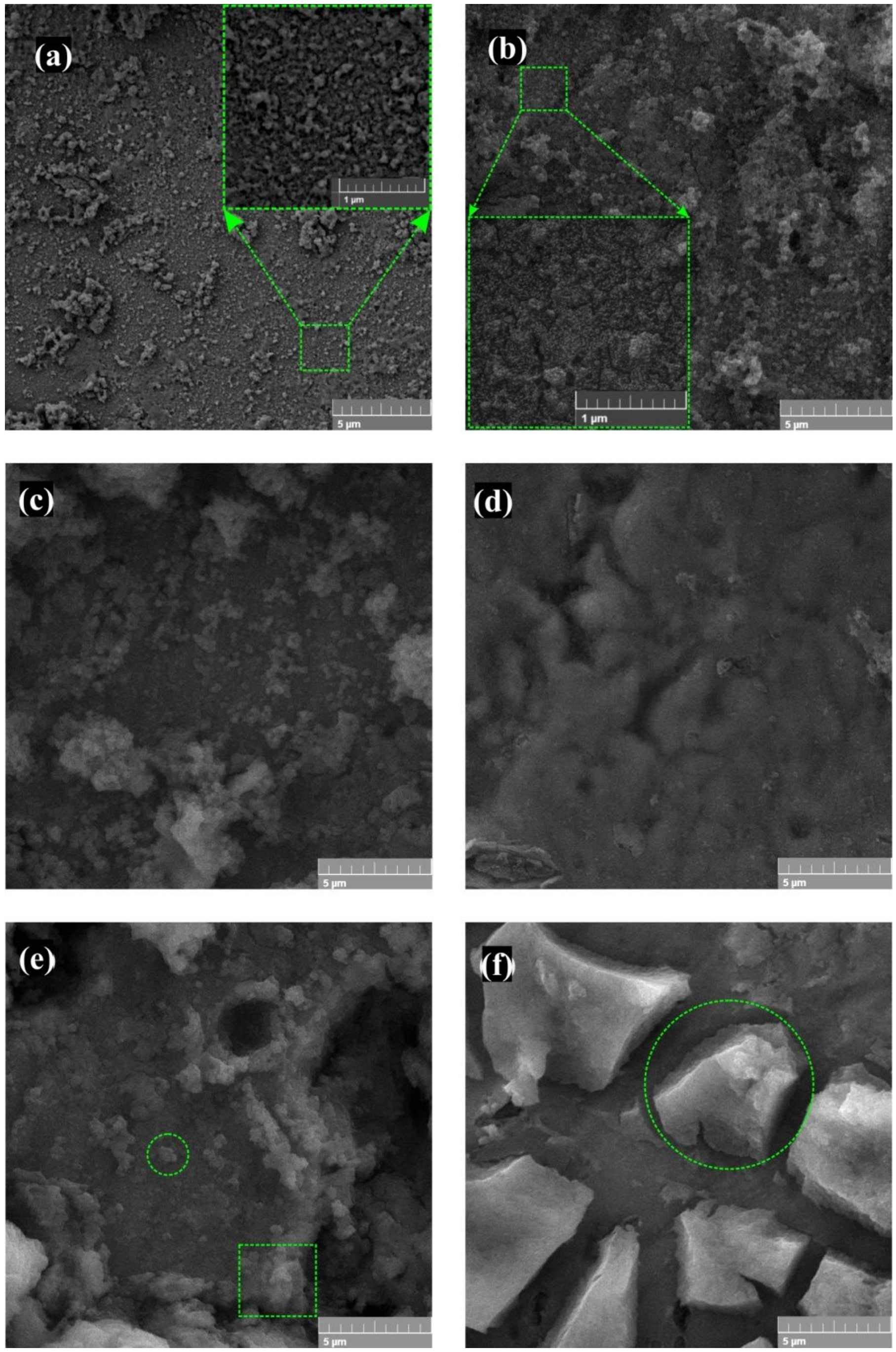

Figure 7. FE-SEM micrographs presenting the morphology of a) ACP/TiO2 and b) ACP+ChOL/TiO2 on Ti; ACP/TiO2 coating on Ti immersed in SBF for c) 72 h and e) 240 h; ACP+ChOL/TiO2 coating on Ti immersed in SBF for: d) 72 and f) 240 h.

SEM images show that the synthesized composite coatings cover the substrate surface area uniformly. The coatings comprise of agglomerated nanosized particles, and the particles have size smaller than 100 nm. Two morphologically different coatings can be observed for ACP/TiO_2 and ACP+ChOL/TiO_2 coatings. The ACP/TiO_2 agglomerates appear larger, thus the surface is being coarser than for ACP+ChOL/TiO_2. Also apparent is the presence of small fractures on the surface of ACP+ChOL/TiO_2 composite coating. In previous research [24] it has been found that the adhesion has highest level of 5 according to ASTM D 3359-02: Standard Test Methods for Measuring Adhesion by Tape; cross-cut tape test (B) without any delamination and without flaking. These findings justify that pores are primarily formed during one step *in situ* anodization/anaphoretic electrodeposition process. Further analyses of the samples were conducted by XRD, and the results are presented in Figure 8.

XRD patterns for ACP/TiO_2 and ACP+ChOL/TiO_2 composite coatings before and after soaking in SBF for 240 h at 37 °C are presented in Figure 8.

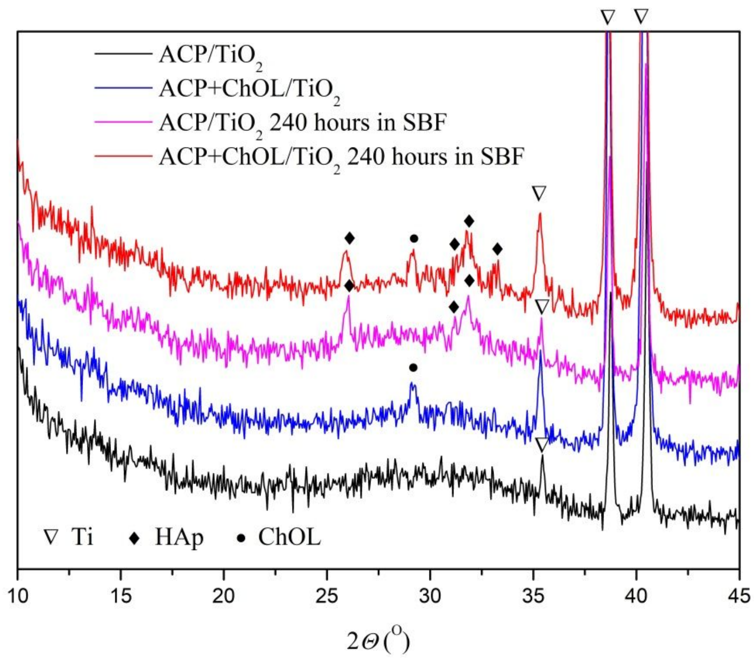

Figure 8. XRD patterns of ACP/TiO_2 and $ACP+ChOL/TiO_2$ composite coatings before and after immersion in SBF for 240 h at 37 ˚C.

As it can be observed in Figure 8, the diffraction pattern of ACP/TiO_2 and $ACP+ChOL/TiO_2$ before and after immersion in SBF for 240 h show typical reflection maximum at about 2θ 30˚ , indicating the main coating component is ACP [24,28,66]. On both $ACP+ChOL/TiO_2$ XRD diffraction patterns (before and after soaking in SBF) diffraction peak at 2θ 29.4˚ can be noticed that can be assigned to chitosan [24,67,68]. Also, XRD diffraction peaks can be observed at ACP/TiO_2 and $ACP+ChOL/TiO_2$ samples after immersion in SBF for 240 h (pink and red difractograms) at 2θ

25.8, 31.3 and 31.85° that can be assigned to (0 0 2), (2 1 1) and (1 1 2) reflections of HAp crystal lattice. For the ACP+ChOL/TiO_2 sample after immersion in SBF one more XRD diffraction peak is present at 2θ 32.9° that corresponds to (3 0 0) reflection from HAp crystal lattice. Newly formed rock-like structures of the size around 5 μm in diameter with smooth surfaces (Figure 7f – circled part) are the most probable reason for appearance of (3 0 0) reflection in difractogram. This proves that crystalline apatite (namely HAp) is deposited onto the surface of both samples after immersion in SBF for 240 h. Hence, single-step *in situ* electrophoretic deposition of nano amorphous calcium phosphate/chitosan oligosaccharide lactate composite coatings with simultaneous production and incorporation of titanium oxide occurs. This composite coating has bioactive and biocompatible properties as well.

By comparing Figures 7a and 7c, it can be seen that 72 h were required for the new apatite layer to start forming onto the ACP/TiO_2 composite surface, while for the ACP+ChOL/TiO_2 composite sample, 72 h were enough for completely being covered with new apatite layer (Figure 7b comparing to Figure 7d). Both statements came from the observation that the morphology of the coatings is different and that visually inspected roughness of the surface is increased. Different morphology of the newly formed apatite layer is because of different size and accessibility of nucleation sites, *i.e.*, available free surface for apatite formation. Since the ACP/TiO_2 coating consists of larger agglomerates of nanosized particles (Figure 7a), and its surface is coarser than the ACP+ChOL/TiO_2 one (Figure 7b), the new apatite layer is formed unevenly on the surface, which hence preferentially grows not in planar direction, but vertical. The ACP+ChOL/TiO_2 coating has larger number of smaller agglomerates as freely available apatite nucleation sites. Consequently, the new apatite layer grows preferentially planar. Uneven distribution of apatite sphere-like particles can be observed on ACP/TiO_2 coating, while this distribution is smooth, even and complete on ACP+ChOL/TiO_2 surface after 72 h of immersion in SBF solution.

Figures 7e and f show the morphologies of ACP/TiO_2 and ACP+ChOL/TiO_2 composite surfaces after 240 h of immersion in SBF solution. What is noticeable straightforwardly is that FE-SEM results confirm bioactivity of both ACP/TiO_2 and ACP+ChOL/TiO_2 composite coatings after immersion in SBF. New apatite layer covers completely the whole sample surface in both cases. The difference between the surfaces of the two samples is also visible. The newly formed apatite layer thoroughly covered the composite surface and thus there is continuation of apatite growth in form of irregular (Figure 7e – squared part), globular, sphere-like particles (Figure 7e – circled part) on ACP/TiO_2 surface. On the other hand, the surface area of ACP+ChOL/TiO_2 surface is completely covered with apatite layer on top of which crystalline HAp is formed, seen as rock-like structures of the size around 5 μm in diameter with smooth surfaces (Figure 7f). Formation of HAp from SBF is among the preliminary supporting evidence for *in vivo* bone bonding capability of the composite-coated Ti. The as-bone apatite formed on the implant surface after immersion in SBF solution appears to aid in cell cascading and protein signaling, which as the result has the formation of bone tissue [44]. It has been determined that the bone-like HAp layer has exceptional osteoconductivity and exhibited excessive affinity with living bone cells [69]. Additionally, it provides for more osteoblast cells to create a whole new bone tissue. Thus, the development of the HAp layer along the surface of implant material is a vital requirement for osseointegration between the living bone tissue and implant.

The considerable bioactivity of both composite coating is verified by the formation of an apatite layer after 240 h of soaking in SBF. Besides, ACP+ChOL/TiO_2 coating has greater bioactivity compared to ACP/TiO_2 coating. The former statements are proven by FE-SEM and XRD analyses.

A cross-sectional SEM image and its corresponding EDS spectra in the case of ACP+ChOL/TiO_2 coating is presented in Figure 9a. A compact structure of the coating with two distinguishable morphologies can be observed. The first morphology, 170±15 μm thick and labeled γ on Figure 9a, belongs to TiO_2 layer, which forms instantaneously when the voltage difference is applied. The EDS measurements (Figure 9a$_2$) show the presence of only Ti and O from TiO_2, with some traces of Ca and P. The second morphology, labeled β on Figure 9a, belongs to ACP+ChOL/TiO_2 coating, whose deposition is diffusion limited process, and it is 120±10 μm thick.

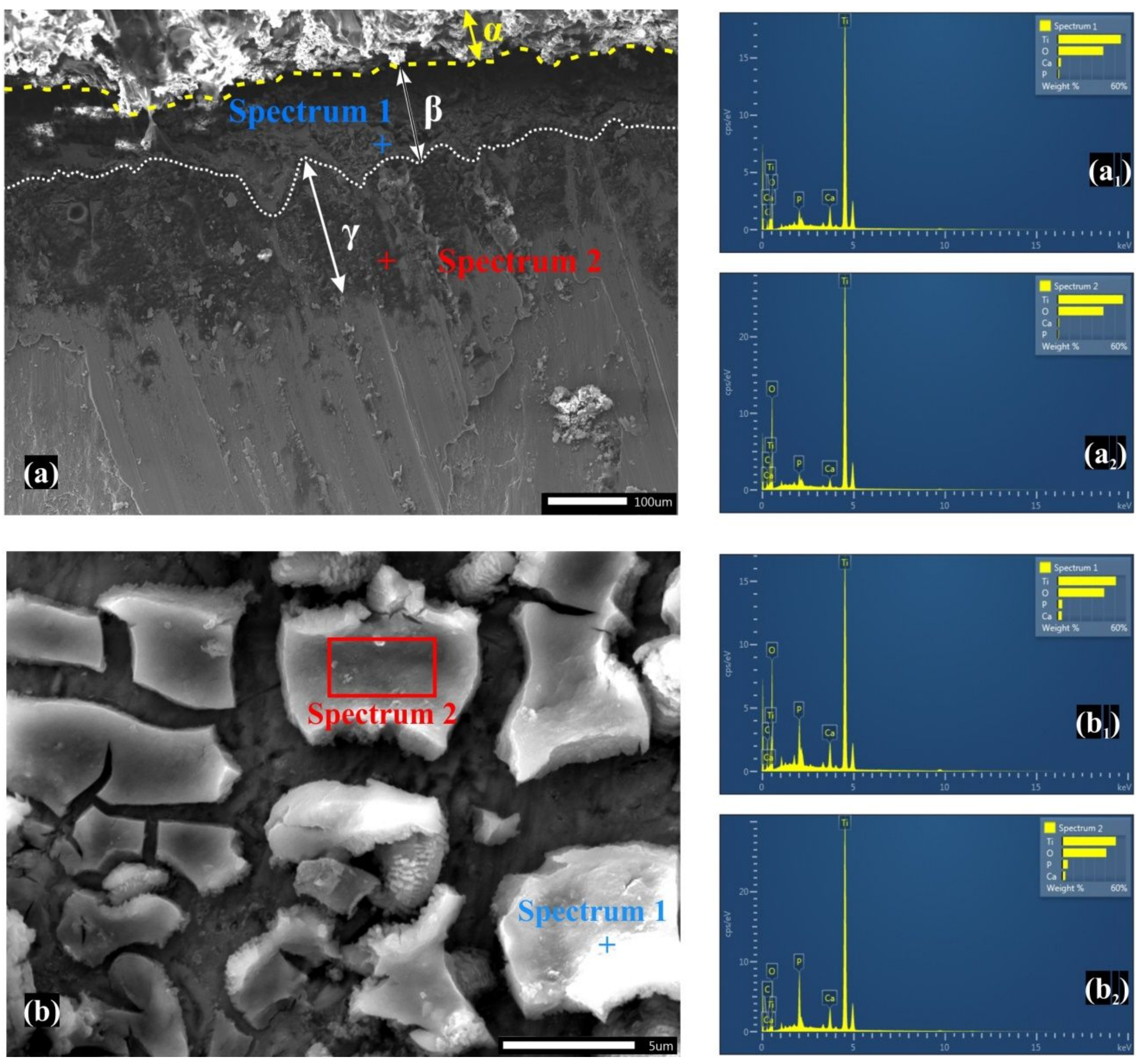

Figure 9. Analysis of sample surfaces a) SEM of cross-section of ACP+ChOL/TiO_2, a_1) EDS Spectrum 1, a_2) EDS Spectrum 2, b) SEM of ACP+ChOL/TiO_2 sample after immersion in SBF for 240 h, b_1) EDS Spectrum 1 and b_2) EDS Spectrum 2

The EDS measurements of layer β (Figure 9a_1) show presence of Ca and P from ACP besides Ti and O from TiO_2 and some C from ChOL. The top layer, labeled as α, belongs to the epoxy resin used to protect the coating while it was cross-cut for the analysis.

ACP/TiO_2 and ACP+ChOL/TiO_2 samples after the immersion in SBF for 240 h were also subjected to EDS analyses in order to determine the composition of formed physiological hydroxyapatite. Figure 9b shows SEM image of the ACP+ChOL/TiO_2 sample after immersion in SBF for 240 h with places where the EDS measurements were performed and the EDS results.

Presence of both Ca and P can be seen from Figure 9$b_{1,2}$. Ca/P ratio of ACP+ChOL/TiO_2 sample was 1.71 for Spectrum 1 and 1.62 for Spectrum 2. For ACP/TiO_2 sample the Ca/P ratio was 1.63. Even though the ideal Ca/P ratio for stoichiometric HAP is known to be 1.67, stable HAp phases have been found to exist over a range of Ca/P ratios between 1.3 and 1.8 [4]. The accurate amount of calcium and phosphate cannot be precisely determined by EDS measurements. However, it proves the presence of CaP phase. Also there is presence of C from ChOL in both spectra in Figure $9b_{1,2}$.. In general, the EDS quantitative measurements are performed during SEM investigations to determine the elemental distribution in the synthesized films and to estimate the Ca/P ratio [70].

3.5. Antibacterial activity

The original hypotheses and driving force of the investigation was the fact that addition of ChOL to ACP coating would yield a material with enhanced corrosion stability, good adhesion and improved antimicrobial properties. It was already proven that both ACP/TiO_2 and ACP+ChOL/TiO_2 coatings on Ti substrate are non-cytotoxic on human lung fibroblast cell line (MRC-5), with ACP+ChOL/TiO_2 coating having improved cell proliferation, differentiation and cell viability [71]. Figures 10a and c illustrate the antibacterial activity of the samples against *S. aureus* and *P. aeruginosa* strains, respectively, while Figures 10b and d present the results of VCC measurements after 420 min for *S. aureus* and *P. aeruginosa* strains, respectively.

Antibacterial activity was evaluated immediately after inoculation, followed by aliquoting after 60, 120, 180, 240, 300, 360 and 420 min of incubation. From the results of antimicrobial activity revealed in Figure 10 it can be observed that cell counts had been slightly retained even up to 180 min post incubation for all the samples when set alongside the initial number of cells in suspension. This particular effect was somewhat more pronounced for the samples tested against *P. aeruginosa* (Figure 10c). After 180 min, there is exponential growth of bacterial film. Both ACP/TiO_2 specimens and pure cp-Ti samples exhibited a similar anti-biofilm activity as control group for both bacterial strains. However, composite samples containing chitosan oligosaccharide lactate (ACP+ChOL/TiO_2) showed improved antimicrobial activity. After 420 min of ACP+ChOL/TiO_2 samples incubation with *P. aeruginosa* PAO1 and *S. aureus* (Figure 10a and c), a decrease in the number of cells was observed for as much as 4 fold for *P. aeruginosa* and 3 fold for *S. aureus*. Generation time had been also increased by about 15 min for *P. aeruginosa* and 9 min for *S. aureus*.

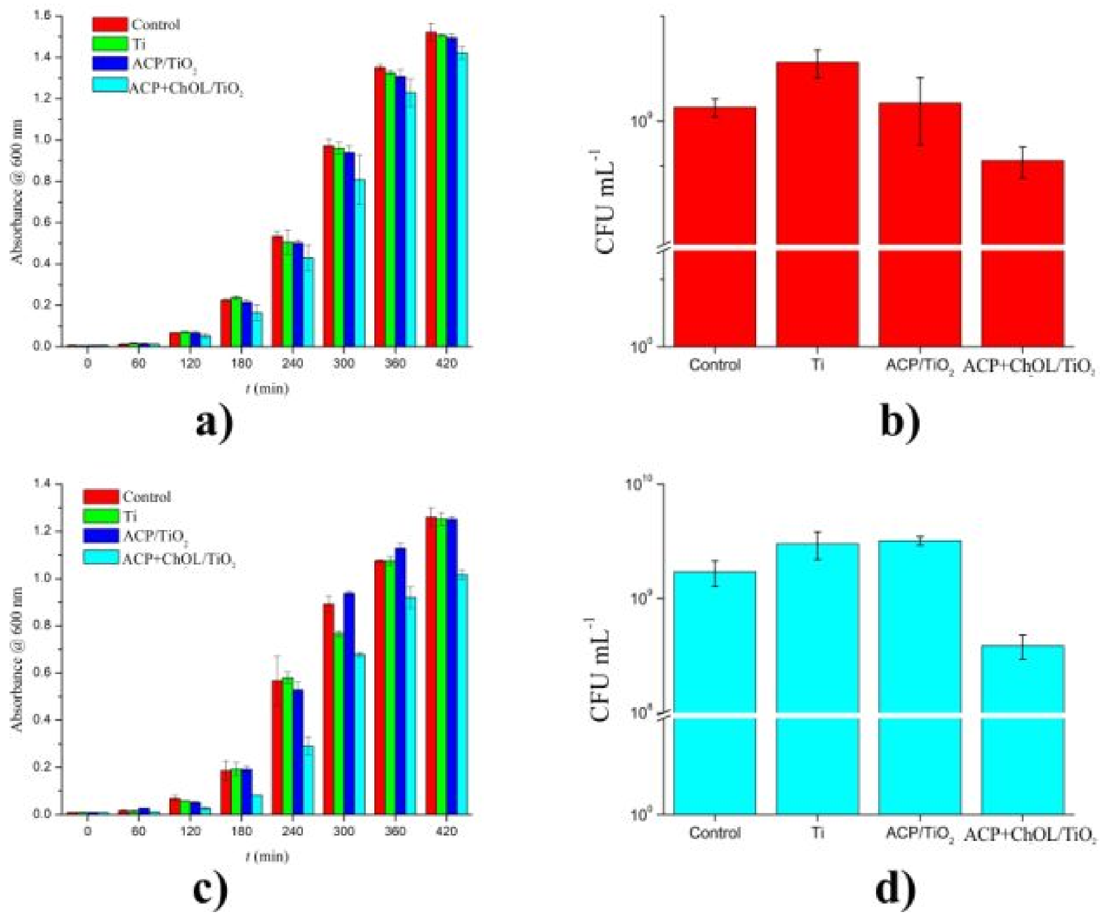

Figure 10. Growth curve measured by optical density measurements for: a) Staphylococcus aureus and c) Pseudomonas aeruginosa PAO1*. Viable cell count after 420 min for: b) Staphylococcus aureus and d) Pseudomonas aeruginosa.

*Measurement at 180 min for ACP+ChOL/TiO2 has error bar, but the error is 7×10^{-4}

Analysis of variance (ANOVA) was performed on antimicrobial activity of control groups, Ti, ACP/TiO_2 and $ACP+ChOL/TiO_2$ coatings to confirm the consistency of the counts at different times. The ANOVA results of antimicrobial activity on *S. aureus* are shown in Table S1 and the ANOVA results of antimicrobial activity on *P. aeruginosa* are shown in Table S2 in Supplementary Material. The analysis showed significant difference at the 5% level of confidence.

Analysis of variance showed significant difference for the counts at 120, 180, 360 and 420 min of incubation for *S. aureus*, and significant difference for the counts at 120, 180, 240, 300, 360 and 420 min of incubation for *P. aeruginosa*.

Results of VCC measurements after 420 min additionally verify the supremacy and bacterial reduction of both bacterial strains, compared to ACP/TiO_2 and pure cp-Ti samples. There is noticeable reduction of *S. aureus* and *P. aeruginosa* cell counts, definitely demonstrating that the ChOL antibacterial potential is conveyed even with such low concentration as 5 mass %.

Chitosan oligosaccharide lactate possesses primary amino groups in its structures. The number of these amino groups has been shown to play a major role in antibacterial activity [72]. The commonly recognized mechanism explains that ChOL has the ability to alter permeability features of microbial cell membrane and further prevent the entry of materials. Otherwise it causes leakage of cell constituents that finally results in death of bacteria [73]. The authors suggest that the site of ChOL action is most likely the bacterial envelope and killing of the organism could be caused by membrane disruption. An additional suggested mechanism for antibacterial activity of ChOL could be the blockade of RNA transcription by adsorption of penetrated ChOL to bacterial DNA [74].

In general, positively charged nature of ChOL molecules facilitates their binding with bacterial cell wall and additionally results with the inhibition of bacterial cell growth. This is due to fact that positively charged amino group at C-2 position of the glucosamine monomer interacts with negatively charged carboxylic acid group of the macromolecules of bacterial cell surface and forms polyelectrolyte complexes [74,75]. This may function as impermeable layer around the cell and suppress the metabolic activity of the bacteria by blocking of nutrient permeation through the cell wall.

It was also revealed that water-soluble ChOL, used in our experiments, exhibit bactericidal activity against both Gram-positive and Gram-negative bacteria [73].

4. CONCLUSIONS

ACP/TiO_2 and ACP+ChOL/TiO_2 composite coatings on anodized Ti have been successfully synthesized by *in situ* method of simultaneous anodization of Ti substrate and anaphoretic deposition of calcium phosphate-based coatings. The obtained hybrid nano composite coatings are around 300±15 μm thick, with 2 distinguishable phases. The first phase is 170±15 μm thick and it belongs to TiO_2, where the second phase belongs to coatings with TiO_2. This phase is 120±10 μm thick. The coatings were subjected to electrochemical corrosion testing, *in vitro* bioactivity testing and antibacterial activity testing.

E_{OCP} measurements show that the potentials of both analyzed composite coatings on titanium were nobler than those of the bare cp-Ti. This finding indicates better surface passivation of the Ti support. ACP+ChOL/TiO_2 composite coating showed the lowest j_{corr} value, which was about three times lower than the corrosion current density value for pure Ti sample. ACP/TiO_2 composite coating exhibited j_{corr} value which was also lower than for bare cp-Ti sample. Better corrosion stability of both ACP/TiO_2 and ACP+ChOL/TiO_2 samples implies that the corrosion behavior and durability of the samples in the SBF medium was highly influenced by the formation of both inhomogeneous and homogeneous oxide, ceramic and composite layers. The inclusion of ChOL into ACP with simultaneous titanium oxide formation helps in the formation of well-bonded uniform stable coating on cp-Ti surface with high corrosion resistance. The nobler E_{corr} and lower j_{corr} values indicate the ability of ACP/TiO_2 and ACP+ChOL/TiO_2 composite coated samples to offer an excellent corrosion resistance for titanium samples for *in vitro* applications. ACP+ChOL/TiO_2 has more homogenous inner passive layer/film, with good adherence to Ti substrate. There is high bioactivity of both ACP/TiO_2 and ACP+ChOL/TiO_2 composite coatings after immersion in SBF which is confirmed by the formation of new apatite layer that completely covers whole surface at both samples. However, the surface of ACP+ChOL/TiO_2 was completely covered by a new apatite layer after 72 h, while ACP/TiO_2 required 168 h. Besides the fact that the ACP+ChOL/TiO_2 showed better corrosion resistivity and higher bioactivity, the unique confirmation of preference of ACP+ChOL/TiO_2 over ACP/TiO_2 coating comes from antibacterial activity testing. A decrease in the number of cells was observed for as much as 4 times for *P. aeruginosa* and 3 times for *S. aureus* for ACP+ChOL/TiO_2 samples with respect to ACP/TiO_2. The findings are confirmed by ANOVA analysis, which showed significant difference at the 5% level of confidence

All of the findings show that ACP+ChOL/TiO_2 has high multifunctional potential which will be the subject of our further investigations. Hence ACP+ChOL/TiO_2 can be considered for further biomedical testing as excellent potential material for medical implant application.

SUPPORTING INFORMATION

Analysis of variance (ANOVA) results of antimicrobial activity on *Staphylococcus aureus,* ATCC 25923 and *Pseudomonas aeruginosa* PAO1, ATCC 15692 in table form

AUTHOR INFORMATION

Corresponding Authors

*** Miroslav M. Pavlović** - Institute of Chemistry, Technology and Metallurgy, Institute of national importance for the Republic of Serbia, University of Belgrade, Belgrade, Serbia; Center of Excellence in Environmental Chemistry and Engineering - ICTM, University of Belgrade, Belgrade, Serbia, e-mail: mpavlovic@tmf.bg.ac.rs, phone: +381 11 3640231

**** Nenad L. Ignjatović -** Institute of Technical Science of the Serbian Academy of Sciences and Arts, Belgrade, Serbia, e-mail: nenad.ignjatovic@itn.sanu.ac.rs, phone: +381 11 2185437

Authors

Marijana R. Pantović Pavlović - Institute of Chemistry, Technology and Metallurgy, Institute of national importance for the Republic of Serbia, University of Belgrade, Belgrade, Serbia; Center of Excellence in Environmental Chemistry and Engineering - ICTM, University of Belgrade, Belgrade, Serbia

Boris P. Stanojević - Faculty of International Engineering Management, Belgrade, Serbia

Vladimir V. Panić - Institute of Chemistry, Technology and Metallurgy, Institute of national importance for the Republic of Serbia, University of Belgrade, Belgrade, Serbia; Center of Excellence in Environmental Chemistry and Engineering - ICTM, University of Belgrade, Belgrade, Serbia; State University of Novi Pazar, Department of Chemical-Technological Sciences, Novi Pazar, Serbia

Marija D. Mihailović - Institute of Chemistry, Technology and Metallurgy, Institute of national importance for the Republic of Serbia, University of Belgrade, Belgrade, Serbia

Jasmina S. Stevanović - Institute of Chemistry, Technology and Metallurgy, Institute of national importance for the Republic of Serbia, University of Belgrade, Belgrade, Serbia; Center of Excellence in Environmental Chemistry and Engineering - ICTM, University of Belgrade, Belgrade, Serbia

Notes

The authors declare that they have no known competing financial interests or personal relationships that could have appeared to influence the work reported in this paper.

ACKNOWLEDGEMENTS

This work was supported by the Ministry of Education, Science and Technological Development of the Republic of Serbia (Grant No. 451-03-9/2021-14/200026 and grant No. 451-03-9/2021-14/200175).

The authors would like to thank Prof. dr Zoran Radojičić from Faculty of Organizational Sciences, University of Belgrade for his considerable contribution to statistical analyses of the data.

REFERENCES

(1) Barjaktarević, D. R.; Djokić, V. R.; Bajat, J. B.; Dimić, I. D.; Cvijović-Alagić, I. L.; Rakin,

M. P. The Influence of the Surface Nanostructured Modification on the Corrosion Resistance of the Ultrafine-Grained Ti–13Nb–13Zr Alloy in Artificial Saliva. *Theor. Appl. Fract. Mech.* **2019**, *103*, 102307. https://doi.org/https://doi.org/10.1016/j.tafmec.2019.102307.

(2) Duraccio, D.; Mussano, F.; Faga, M. G. Biomaterials for Dental Implants: Current and Future Trends. *J. Mater. Sci.* **2015**, *50* (14), 4779–4812. https://doi.org/10.1007/s10853-015-9056-3.

(3) Liu, X.; Chu, P. K.; Ding, C. Surface Modification of Titanium, Titanium Alloys, and Related Materials for Biomedical Applications. *Mater. Sci. Eng. R Reports* **2004**, *47* (3–4), 49–121. https://doi.org/http://dx.doi.org/10.1016/j.mser.2004.11.001.

(4) Pantović Pavlović, M. R.; Eraković, S. G.; Pavlović, M. M.; Stevanović, J. S.; Panić, V. V.; Ignjatović, N. L. Anaphoretical/Oxidative Approach to the in-Situ Synthesis of Adherent Hydroxyapatite/Titanium Oxide Composite Coatings on Titanium. *Surf. Coatings Technol.* **2019**, *358*, 688–694. https://doi.org/10.1016/j.surfcoat.2018.12.003.

(5) Ahmadi, S.; Sadrnezhaad, S. K. A Novel Method for Production of Foamy Core@compact

Shell Ti6Al4V Bone-like Composite. *J. Alloys Compd.* **2016**, *656*, 416–422. https://doi.org/http://dx.doi.org/10.1016/j.jallcom.2015.09.248.

(6) Long, M.; Rack, H. J. Titanium Alloys in Total Joint Replacement—a Materials Science Perspective. *Biomaterials* **1998**, *19* (18), 1621–1639. https://doi.org/http://dx.doi.org/10.1016/S0142-9612(97)00146-4.

(7) Dezfuli, S. N.; Sadrnezhaad, S. K.; Shokrgozar, M. A.; Bonakdar, S. Fabrication of Biocompatible Titanium Scaffolds Using Space Holder Technique. *J. Mater. Sci. Mater. Med.* **2012**, *23* (10), 2483–2488. https://doi.org/10.1007/s10856-012-4706-3.

(8) Geetha, M.; Singh, A. K.; Asokamani, R.; Gogia, A. K. Ti Based Biomaterials, the Ultimate Choice for Orthopaedic Implants – A Review. *Prog. Mater. Sci.* **2009**, *54* (3), 397–425. https://doi.org/https://doi.org/10.1016/j.pmatsci.2008.06.004.

(9) Ahmadi, S.; Mohammadi, I.; Sadrnezhaad, S. K. Hydroxyapatite Based and Anodic Titania Nanotube Biocomposite Coatings: Fabrication, Characterization and Electrochemical Behavior. *Surf. Coatings Technol.* **2016**, *287*, 67–75. https://doi.org/http://dx.doi.org/10.1016/j.surfcoat.2015.12.062.

(10) Benea, L.; Danaila, E.; Ponthiaux, P. Effect of Titania Anodic Formation and Hydroxyapatite Electrodeposition on Electrochemical Behaviour of Ti–6Al–4V Alloy under Fretting Conditions for Biomedical Applications. *Corros. Sci.* **2015**, *91*, 262–271. https://doi.org/https://doi.org/10.1016/j.corsci.2014.11.026.

(11) Chiang, C.-Y.; Chiou, S.-H.; Yang, W.-E.; Hsu, M.-L.; Yung, M.-C.; Tsai, M.-L.; Chen, L.-K.; Huang, H.-H. Formation of TiO2 Nano-Network on Titanium Surface Increases the Human Cell Growth. *Dent. Mater.* **2009**, *25* (8), 1022–1029. https://doi.org/https://doi.org/10.1016/j.dental.2009.03.001.

(12) Pantovic-Pavlovic, M.; Pavlovic, M.; Erakovic, S.; Barudzija, T.; Stevanovic, J.; Ignjatovic, N.; Panic, V. Relationship between the Properties of an Interlayer Formed by in Situ Ti Anodization and Anaphoretically Deposited Hydroxyapatite. *J. Serbian Chem. Soc.* **2019**, *84* (11), 1305–1318. https://doi.org/10.2298/jsc190730105p.

(13) Han, C.; Wang, Q.; Song, B.; Li, W.; Wei, Q.; Wen, S.; Liu, J.; Shi, Y. Microstructure and Property Evolutions of Titanium/Nano-Hydroxyapatite Composites in-Situ Prepared by Selective Laser Melting. *J. Mech. Behav. Biomed. Mater.* **2017**, *71*, 85–94.

https://doi.org/http://dx.doi.org/10.1016/j.jmbbm.2017.02.021.

(14) Hamada, K.; Kon, M.; Hanawa, T.; Yokoyama, K.; Miyamoto, Y.; Asaoka, K. Hydrothermal Modification of Titanium Surface in Calcium Solutions. *Biomaterials* **2002**, *23* (10), 2265–2272. https://doi.org/http://dx.doi.org/10.1016/S0142-9612(01)00361-1.

(15) Osman, R.; Swain, M. A Critical Review of Dental Implant Materials with an Emphasis on Titanium versus Zirconia. *Materials (Basel).* **2015**, *8* (3), 932.

(16) Jäger, M.; Jennissen, H. P.; Dittrich, F.; Fischer, A.; Köhling, H. L. Antimicrobial and Osseointegration Properties of Nanostructured Titanium Orthopaedic Implants. *Materials* . 2017. https://doi.org/10.3390/ma10111302.

(17) Kulkarni, M.; Mazare, A.; Schmuki, P.; Iglič, A. Biomaterial Surface Modification of Titanium and Titanium Alloys for Medical Applications. *Nanomedicine* **2014**, *111*, 111.

(18) Gilabert-Chirivella, E.; Pérez-Feito, R.; Ribeiro, C.; Ribeiro, S.; Correia, D. M.; González-Martín, M. L.; Manero, J. M.; Lanceros-Méndez, S.; Ferrer, G. G.; Gómez-Ribelles, J. L. Chitosan Patterning on Titanium Implants. *Prog. Org. Coatings* **2017**, *111*, 23–28. https://doi.org/https://doi.org/10.1016/j.porgcoat.2017.04.027.

(19) Ferraris, S.; Spriano, S. Antibacterial Titanium Surfaces for Medical Implants. *Mater. Sci. Eng. C* **2016**, *61*, 965–978. https://doi.org/https://doi.org/10.1016/j.msec.2015.12.062.

(20) Simchi, A.; Tamjid, E.; Pishbin, F.; Boccaccini, A. R. Recent Progress in Inorganic and Composite Coatings with Bactericidal Capability for Orthopaedic Applications. *Nanomedicine Nanotechnology, Biol. Med.* **2011**, *7* (1), 22–39. https://doi.org/https://doi.org/10.1016/j.nano.2010.10.005.

(21) Chen, M.; Li, H.; Wang, X.; Qin, G.; Zhang, E. Improvement in Antibacterial Properties and Cytocompatibility of Titanium by Fluorine and Oxygen Dual Plasma-Based Surface Modification. *Appl. Surf. Sci.* **2019**, *463*, 261–274. https://doi.org/https://doi.org/10.1016/j.apsusc.2018.08.194.

(22) Kang, K.; Zakiyuddin, A.; Lee, K. Electrochemical Properties of HA Coated Titanium Dioxide Nanotubes. *J. Nanosci. Nanotechnol.* **2016**, *16* (2), 1708–1710. https://doi.org/10.1166/jnn.2016.11988.

(23) Yilmaz, B.; Evis, Z.; Tezcaner, A.; Banerjee, S. Surface Characterization and Biocompatibility of Selenium-Doped Hydroxyapatite Coating on Titanium Alloy. *Int. J.*

Appl. Ceram. Technol. **2016**, *13* (6), 1059–1068. https://doi.org/10.1111/ijac.12577.

(24) Pantović Pavlović, M. R.; Pavlović, M. M.; Eraković, S.; Stevanović, J. S.; Panić, V. V; Ignjatović, N. Simultaneous Anodization/Anaphoretic Electrodeposition Synthesis of Nano Calcium Phosphate/Titanium Oxide Composite Coatings Assisted with Chitosan Oligosaccharide Lactate. *Mater. Lett.* **2020**, *261*, 127121. https://doi.org/10.1016/j.matlet.2019.127121.

(25) Moore, B.; Asadi, E.; Lewis, G. Deposition Methods for Microstructured and Nanostructured Coatings on Metallic Bone Implants: A Review. *Adv. Mater. Sci. Eng.* **2017**, *2017*, 9. https://doi.org/10.1155/2017/5812907.

(26) V. Dorozhkin, S. Amorphous Calcium Orthophosphates: Nature, Chemistry and Biomedical Applications. *Int. J. Mater. Chem.* **2012**, *2* (1), 19–46. https://doi.org/10.5923/j.ijmc.20120201.04.

(27) Ignjatović, N. L.; Sakač, M.; Kuzminac, I.; Kojić, V.; Marković, S.; Vasiljević-Radović, D.; Wu, V. M.; Uskoković, V.; Uskoković, D. P. Chitosan Oligosaccharide Lactate Coated Hydroxyapatite Nanoparticles as a Vehicle for the Delivery of Steroid Drugs and the

Targeting of Breast Cancer Cells. *J. Mater. Chem. B* **2018**, *6* (43), 6957–6968. https://doi.org/10.1039/c8tb01995a.

(28) Du, L. W.; Bian, S.; Gou, B. Di; Jiang, Y.; Huang, J.; Gao, Y. X.; Zhao, Y. D.; Wen, W.; Zhang, T. L.; Wang, K. Structure of Clusters and Formation of Amorphous Calcium Phosphate and Hydroxyapatite: From the Perspective of Coordination Chemistry. *Cryst. Growth Des.* **2013**, *13* (7), 3103–3109. https://doi.org/10.1021/cg400498j.

(29) Pang, X.; Casagrande, T.; Zhitomirsky, I. Electrophoretic Deposition of Hydroxyapatite-CaSiO3-Chitosan Composite Coatings. *J. Colloid Interface Sci.* **2009**, *330* (2), 323–329. https://doi.org/10.1016/j.jcis.2008.10.070.

(30) Sun, F.; Pang, X.; Zhitomirsky, I. Electrophoretic Deposition of Composite Hydroxyapatite-Chitosan-Heparin Coatings. *J. Mater. Process. Technol.* **2009**, *209* (3), 1597–1606. https://doi.org/10.1016/j.jmatprotec.2008.04.007.

(31) Pawlik, A.; Rehman, M. A. U.; Nawaz, Q.; Bastan, F. E.; Sulka, G. D.; Boccaccini, A. R. Fabrication and Characterization of Electrophoretically Deposited Chitosan-Hydroxyapatite Composite Coatings on Anodic Titanium Dioxide Layers. *Electrochim.*

Acta **2019**, *307*, 465–473. https://doi.org/10.1016/j.electacta.2019.03.195.

(32) Govindharajulu, J. P.; Chen, X.; Li, Y.; Rodriguez-cabello, J. C. Chitosan-Recombinamer Layer-by-Layer Coatings for Multifunctional Implants. *Int. J. Mlecular Sci.* **2017**, *18* (2), 1–16. https://doi.org/10.3390/ijms18020369.

(33) Moskalewicz, T.; Warcaba, M.; Cieniek, Ł.; Sitarz, M.; Gajewska, M.; Boccaccini, A. R. Hydroxyapatite/Sodium Alginate Coatings Electrophoretically Deposited on Titanium Substrates: Microstructure and Properties. *Appl. Surf. Sci.* **2020**, 148353. https://doi.org/https://doi.org/10.1016/j.apsusc.2020.148353.

(34) Yang, Y.; Wang, G.; Zhu, G.; Xu, X.; Pan, H.; Tang, R. The Effect of Amorphous Calcium Phosphate on Protein Protection against Thermal Denaturation. *Chem. Commun.* **2015**, *51* (41), 8705–8707. https://doi.org/10.1039/c5cc01420d.

(35) Blanda, G.; Brucato, V.; Carfì, F.; Conoscenti, G.; La Carrubba, V.; Piazza, S.; Sunseri, C.; Inguanta, R. Chitosan-Coating Deposition via Galvanic Coupling. *ACS Biomater. Sci. Eng.* **2019**, *5* (4), 1715–1724. https://doi.org/10.1021/acsbiomaterials.8b01548.

(36) Boccaccini, A. R.; Keim, S.; Ma, R.; Li, Y.; Zhitomirsky, I. Electrophoretic Deposition of

Biomaterials. *J. R. Soc. Interface* **2010**, *7* (suppl_5), S581–S613. https://doi.org/10.1098/rsif.2010.0156.focus.

(37) Besra, L.; Liu, M. A Review on Fundamentals and Applications of Electrophoretic Deposition (EPD). *Prog. Mater. Sci.* **2007**, *52* (1), 1–61. https://doi.org/https://doi.org/10.1016/j.pmatsci.2006.07.001.

(38) Aydın, İ.; Bahçepınar, A. İ.; Kırman, M.; Çipiloğlu, M. A. HA Coating on Ti6Al7Nb Alloy Using an Electrophoretic Deposition Method and Surface Properties Examination of the Resulting Coatings. *Coatings* **2019**, *9* (6), 402. https://doi.org/10.3390/coatings9060402.

(39) Farrokhi-Rad, M. Electrophoretic Deposition of Hydroxyapatite Fiber Reinforced Hydroxyapatite Matrix Nanocomposite Coatings. *Surf. Coatings Technol.* **2017**, *329*, 155–162. https://doi.org/https://doi.org/10.1016/j.surfcoat.2017.09.051.

(40) Jiang, T.; Zhang, Z.; Zhou, Y.; Liu, Y.; Wang, Z.; Tong, H.; Shen, X.; Wang, Y. Surface Functionalization of Titanium with Chitosan/Gelatin via Electrophoretic Deposition: Characterization and Cell Behavior. *Biomacromolecules* **2010**, *11* (5), 1254–1260. https://doi.org/10.1021/bm100050d.

(41) Blackwood, D. J.; Chua, A. W. C.; Seah, K. H. W.; Thampuran, R.; Teoh, S. H. Corrosion Behaviour of Porous Titanium–Graphite Composites Designed for Surgical Implants. *Corros. Sci.* **2000**, *42* (3), 481–503. https://doi.org/https://doi.org/10.1016/S0010-938X(99)00103-1.

(42) Oyane, A.; Kim, H.-M.; Furuya, T.; Kokubo, T.; Miyazaki, T.; Nakamura, T. Preparation and Assessment of Revised Simulated Body Fluids. *J. Biomed. Mater. Res. Part A* **2003**, *65A* (2), 188–195. https://doi.org/10.1002/jbm.a.10482.

(43) Kokubo, T.; Kim, H. M.; Kawashita, M.; Nakamura, T. Bioactive Metals: Preparation and Properties. *J. Mater. Sci. Mater. Med.* **2004**, *15* (2), 99–107. https://doi.org/10.1023/B:JMSM.0000011809.36275.0c.

(44) Kokubo, T.; Takadama, H. How Useful Is SBF in Predicting in Vivo Bone Bioactivity? *Biomaterials* **2006**, *27* (15), 2907–2915. https://doi.org/https://doi.org/10.1016/j.biomaterials.2006.01.017.

(45) Pavlović, M. M.; Pavlović, M. G.; Panić, V.; Talijan, N.; Vasiljević, L.; Tomić, M. V. Electrical Conductivity of Lignocellulose Composites Loaded with Electrodeposited

Copper Powders. Part III. Influence of Particle Morphology on Appearance of Electrical Conductive Layers. *Int. J. Electrochem. Sci.* **2012**, *7* (9), 8894–8904.

(46) Pavlović, M. M.; Pavlović, M. G.; Cosović, V.; Bojanić, V.; Nikolić, N. D.; Aleksić, R. Influence of Electrolytic Copper Powder Particle Morphology on Electrical Conductivity of Lignocellulose Composites and Formation of Conductive Pathways. *Int. J. Electrochem. Sci.* **2014**, *9* (12), 8355–8366.

(47) REHMAN, I.; BONFIELD, W. Characterization of Hydroxyapatite and Carbonated Apatite by Photo Acoustic FTIR Spectroscopy. *J. Mater. Sci. Mater. Med.* **1997**, *8* (1), 1–4. https://doi.org/10.1023/A:1018570213546.

(48) Kong, W.; Zhao, K.; Gao, C.; Zhu, P. Synthesis and Characterization of Carbonated Hydroxyapatite with Layered Structure. *Mater. Lett.* **2019**, *255*, 126552. https://doi.org/10.1016/j.matlet.2019.126552.

(49) Reyes-Gasga, J.; Martínez-Piñeiro, E. L.; Rodríguez-Álvarez, G.; Tiznado-Orozco, G. E.; García-García, R.; Brès, E. F. XRD and FTIR Crystallinity Indices in Sound Human Tooth Enamel and Synthetic Hydroxyapatite. *Mater. Sci. Eng. C* **2013**, *33* (8), 4568–4574.

https://doi.org/https://doi.org/10.1016/j.msec.2013.07.014.

(50) Koutsopoulos, S. Synthesis and Characterization of Hydroxyapatite Crystals: A Review Study on the Analytical Methods. *J. Biomed. Mater. Res.* **2002**, *62* (4), 600–612. https://doi.org/10.1002/jbm.10280.

(51) López, F. A.; Mercê, A. L. R.; Alguacil, F. J.; López-Delgado, A. A Kinetic Study on the Thermal Behaviour of Chitosan. *J. Therm. Anal. Calorim.* **2008**, *91* (2), 633–639. https://doi.org/10.1007/s10973-007-8321-3.

(52) Wanjun, T.; Cunxin, W.; Donghua, C. Kinetic Studies on the Pyrolysis of Chitin and Chitosan. *Polym. Degrad. Stab.* **2005**, *87* (3), 389–394. https://doi.org/https://doi.org/10.1016/j.polymdegradstab.2004.08.006.

(53) Gebhardt, F.; Seuss, S.; Turhan, M. C.; Hornberger, H.; Virtanen, S.; Boccaccini, A. R. Characterization of Electrophoretic Chitosan Coatings on Stainless Steel. *Mater. Lett.* **2012**, *66* (1), 302–304. https://doi.org/https://doi.org/10.1016/j.matlet.2011.08.088.

(54) Geetha, V.; Gomathi, T.; Sudha, P. N. Preparation and Characterization of Graphene-Grafted-Chitosan/Hydroxyapatite Composite. *J. Chem. Pharm. Res.* **2015**, *7* (5), 871–876.

(55) Tang, S.; Tian, B.; Guo, Y.-J.; Zhu, Z.-A.; Guo, Y.-P. Chitosan/Carbonated Hydroxyapatite Composite Coatings: Fabrication, Structure and Biocompatibility. *Surf. Coatings Technol.* **2014**, *251*, 210–216. https://doi.org/https://doi.org/10.1016/j.surfcoat.2014.04.028.

(56) Oliveira, N. T. C.; Ferreira, E. A.; Duarte, L. T.; Biaggio, S. R.; Rocha-Filho, R. C.; Bocchi, N. Corrosion Resistance of Anodic Oxides on the Ti–50Zr and Ti–13Nb–13Zr Alloys. *Electrochim. Acta* **2006**, *51* (10), 2068–2075. https://doi.org/https://doi.org/10.1016/j.electacta.2005.07.015.

(57) Ren, S.; Du, C.; Liu, Z.; Li, X.; Xiong, J.; Li, S. Effect of Fluoride Ions on Corrosion Behaviour of Commercial Pure Titanium in Artificial Seawater Environment. *Appl. Surf. Sci.* **2020**, *506*, 144759. https://doi.org/https://doi.org/10.1016/j.apsusc.2019.144759.

(58) Yu, S. Y.; Brodrick, C. W.; Ryan, M. P.; Scully, J. R. Effects of Nb and Zr Alloying Additions on the Activation Behavior of Ti in Hydrochloric Acid. *J. Electrochem. Soc.* **1999**, *146* (12), 4429–4438. https://doi.org/10.1149/1.1392655.

(59) Fekry, A. M. The Influence of Chloride and Sulphate Ions on the Corrosion Behavior of Ti and Ti-6Al-4V Alloy in Oxalic Acid. *Electrochim. Acta* **2009**, *54* (12), 3480–3489.

https://doi.org/https://doi.org/10.1016/j.electacta.2008.12.060.

(60) Rikhari, B.; Pugal Mani, S.; Rajendran, N. Electrochemical Behavior of Polypyrrole/Chitosan Composite Coating on Ti Metal for Biomedical Applications. *Carbohydr. Polym.* **2018**, *189*, 126–137. https://doi.org/https://doi.org/10.1016/j.carbpol.2018.01.042.

(61) Elangovan, N.; Srinivasan, A.; Pugalmani, S.; Rajendiran, N.; Rajendran, N. Development of Poly(Vinylcarbazole)/Alumina Nanocomposite Coatings for Corrosion Protection of 316L Stainless Steel in 3.5% NaCl Medium. *J. Appl. Polym. Sci.* **2017**, *134* (27), 44937. https://doi.org/10.1002/app.44937.

(62) Vathsala, K.; Venkatesha, T. V; Praveen, B. M.; Nayana, K. O. Electrochemical Generation of Zn-Chitosan Composite Coating on Mild Steel and Its Corrosion Studies. *Engineering* **2010**, *2* (8), 580–584.

(63) Turelli, F.; Strigin, A. T.; Belinkii, A. L.; Adugina, N. A.; Dmitriev, M. A.; Krutikov, A. N. Simultaneous Determination of Instantaneous Corrosion Rates and Tafel Slopes from Polarization Resistance Measurements. *J. Electrochem. Soc.* **1972**, *120* (4), 6–9.

(64) Saji, V. S.; Choe, H. C.; Brantley, W. A. An Electrochemical Study on Self-Ordered Nanoporous and Nanotubular Oxide on Ti–35Nb–5Ta–7Zr Alloy for Biomedical Applications. *Acta Biomater.* **2009**, *5* (6), 2303–2310. https://doi.org/https://doi.org/10.1016/j.actbio.2009.02.017.

(65) Dimić, I.; Cvijović-Alagić, I.; Hohenwarter, A.; Pippan, R.; Kojić, V.; Bajat, J.; Rakin, M. Electrochemical and Biocompatibility Examinations of High-Pressure Torsion Processed Titanium and Ti–13Nb–13Zr Alloy. *J. Biomed. Mater. Res. Part B Appl. Biomater.* **2018**, *106* (3), 1097–1107. https://doi.org/10.1002/jbm.b.33919.

(66) Pakravanan, K.; Rezaee Roknabadi, M.; Farzanegan, F.; Hashemzadeh, A.; Darroudi, M. Amorphous Calcium Phosphate Nanoparticles-Based Mouthwash: Preparation, Characterization, and Anti-Bacterial Effects. *Green Chem. Lett. Rev.* **2019**, *12* (3), 278–285. https://doi.org/10.1080/17518253.2019.1643412.

(67) Zhou, W.; Wang, Y.; Jian, J.; Song, S. Self-Aggregated Nanoparticles Based on Amphiphilic Poly(Lactic Acid)-Grafted-Chitosan Copolymer for Ocular Delivery of Amphotericin B. *Int. J. Nanomedicine* **2013**, *8*, 3715–3728.

https://doi.org/10.2147/IJN.S51186.

(68) Lai, C.; Chen, Y.; Zhang, S. Study on Chitosan-Lactate Sponges with Oriented Pores as Potential Wound Dressing. *Mater. Sci. Appl.* **2013**, *04* (08), 458–470. https://doi.org/10.4236/msa.2013.48056.

(69) Kumar, A. M.; Suresh, B.; Das, S.; Obot, I. B.; Adesina, A. Y.; Ramakrishna, S. Promising Bio-Composites of Polypyrrole and Chitosan: Surface Protective and in Vitro Biocompatibility Performance on 316L SS Implants. *Carbohydr. Polym.* **2017**, *173*, 121–130. https://doi.org/https://doi.org/10.1016/j.carbpol.2017.05.083.

(70) Duta, L.; Popescu, A. C. Current Status on Pulsed Laser Deposition of Coatings from Animal-Origin Calcium Phosphate Sources. *Coatings* **2019**, *9* (5). https://doi.org/10.3390/coatings9050335.

(71) Pantović Pavlović, M.; Pavlović, M. M.; Kovačina, J.; Stanojević, B.; Stevanović, J.; Panić, V.; Ignjatović, N. Cytotoxicity of Amorphous Calcium Phosphate Multifunctional Composite Coatings on Titanium Obtained by in Situ Anodization/Anaphoretic Deposition: Note. *J. Serbian Chem. Soc.* **2021**, No. SE-. https://doi.org/10.2298/JSC210211024P.

(72) Kim, S.-K.; Rajapakse, N. Enzymatic Production and Biological Activities of Chitosan Oligosaccharides (COS): A Review. *Carbohydr. Polym.* **2005**, *62* (4), 357–368. https://doi.org/https://doi.org/10.1016/j.carbpol.2005.08.012.

(73) Sudarshan, N. R.; Hoover, D. G.; Knorr, D. Antibacterial Action of Chitosan. *Food Biotechnol.* **1992**, *6* (3), 257–272. https://doi.org/10.1080/08905439209549838.

(74) Kim, J. Y.; Lee, J. K.; Lee, T. S.; Park, W. H. Synthesis of Chitooligosaccharide Derivative with Quaternary Ammonium Group and Its Antimicrobial Activity against Streptococcus Mutans. *Int. J. Biol. Macromol.* **2003**, *32* (1), 23–27. https://doi.org/https://doi.org/10.1016/S0141-8130(03)00021-7.

(75) Choi, B.-K.; Kim, K.-Y.; Yoo, Y.-J.; Oh, S.-J.; Choi, J.-H.; Kim, C.-Y. In Vitro Antimicrobial Activity of a Chitooligosaccharide Mixture against Actinobacillus Actinomycetemcomitans and Streptococcus Mutans. *Int. J. Antimicrob. Agents* **2001**, *18* (6), 553–557. https://doi.org/https://doi.org/10.1016/S0924-8579(01)00434-4.

For Table of Contents Use Only

Anodizing/anaphoretic electrodeposition of nano calcium phosphate/chitosan lactate multifunctional coatings on titanium with advanced corrosion resistance, bioactivity and antibacterial properties

Marijana R. Pantović Pavlović, Boris P. Stanojević, Miroslav M. Pavlović, Marija D. Mihailović, Jasmina S. Stevanović, Vladimir V. Panić, Nenad L. Ignjatović

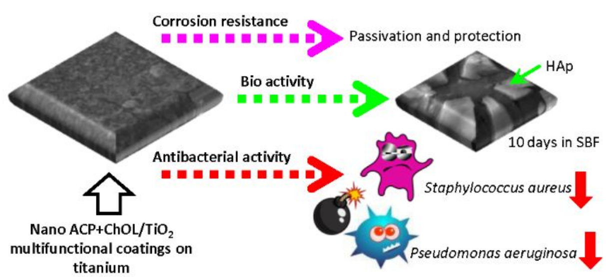

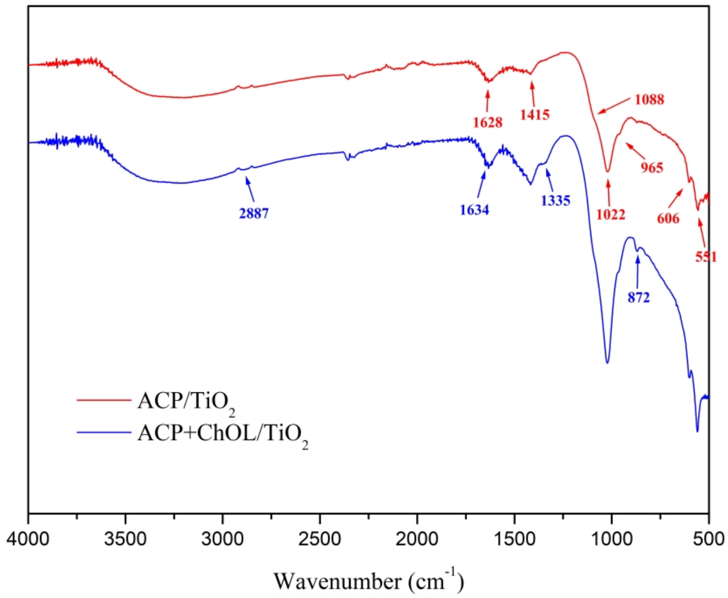

Figure 1. FTIR spectra of ACP/TiO_2 and ACP+ChOL/TiO_2 composite coatings on titanium substrate.

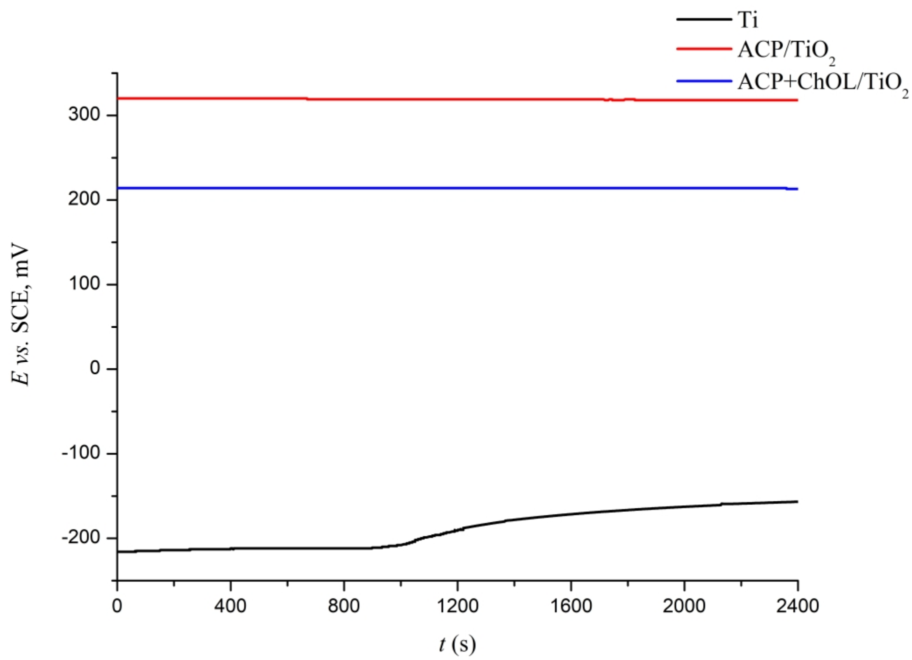

Figure 2. Results of OCP measurements of bare Ti, ACP/TiO_2 and $ACP+ChOL/TiO_2$ composite coatings on titanium during 2400s.

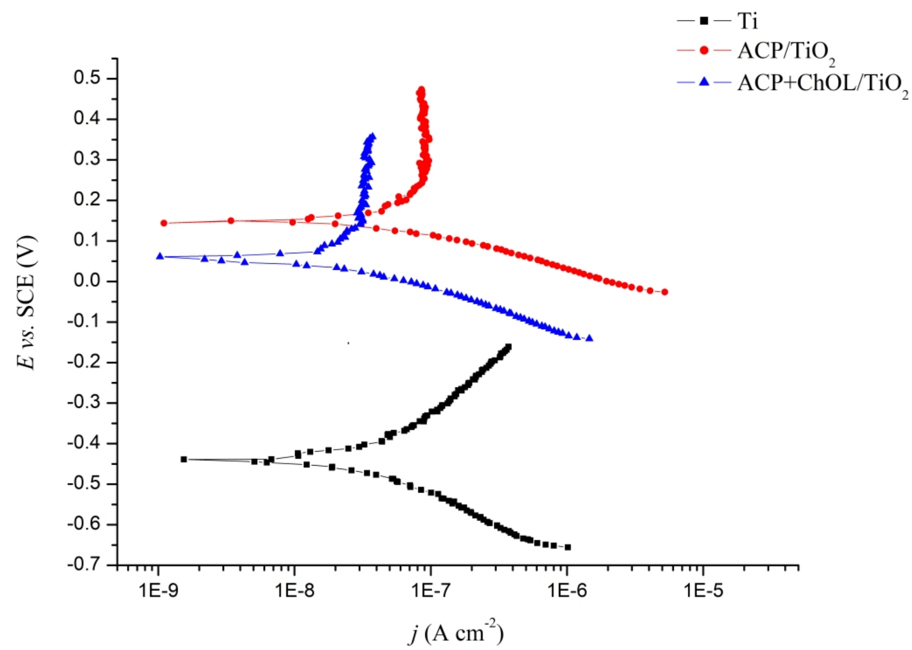

Figure 3. The potentiodynamic polarization curves of bare Ti, ACP/TiO_2 and $ACP+ChOL/TiO_2$ composite coatings on titanium measured from a cathodic potential of −250 mV to an anodic potential of +250 mV in SBF

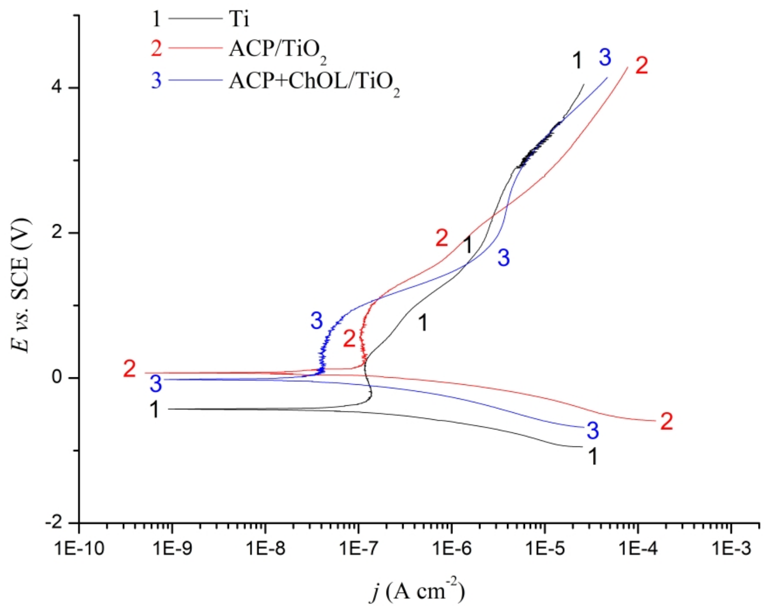

Figure 4. The potentiodynamic polarization curves of bare Ti, ACP/TiO_2 and ACP+ChOL/TiO_2 composite coatings on titanium measured from a cathodic potential of −1 V to an anodic potential of +4 V in SBF

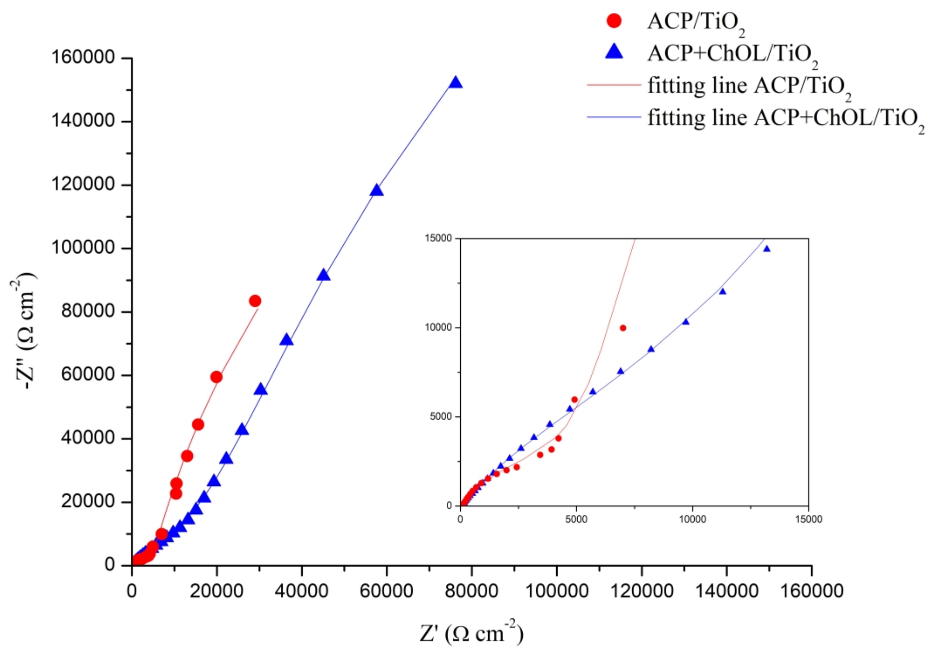

Figure 5. The complex plane plots of ACP/TiO_2 and ACP+ChOL/TiO_2 composite coatings on titanium.

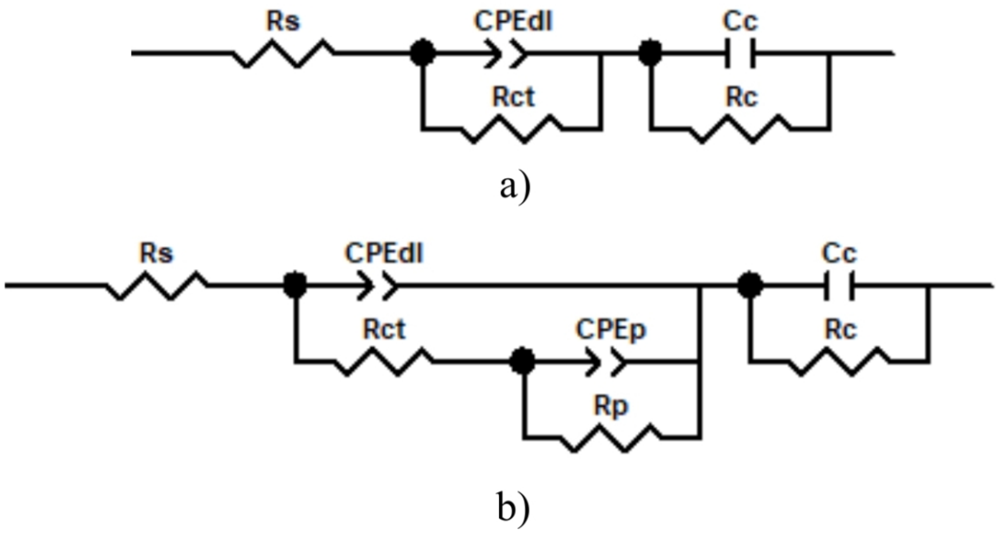

Figure 6. The equivalent electrical circuits used to fit the impedance spectra of: a) ACP/TiO_2 and b) ACP+ChOL/TiO_2 multifunctional composite coatings.

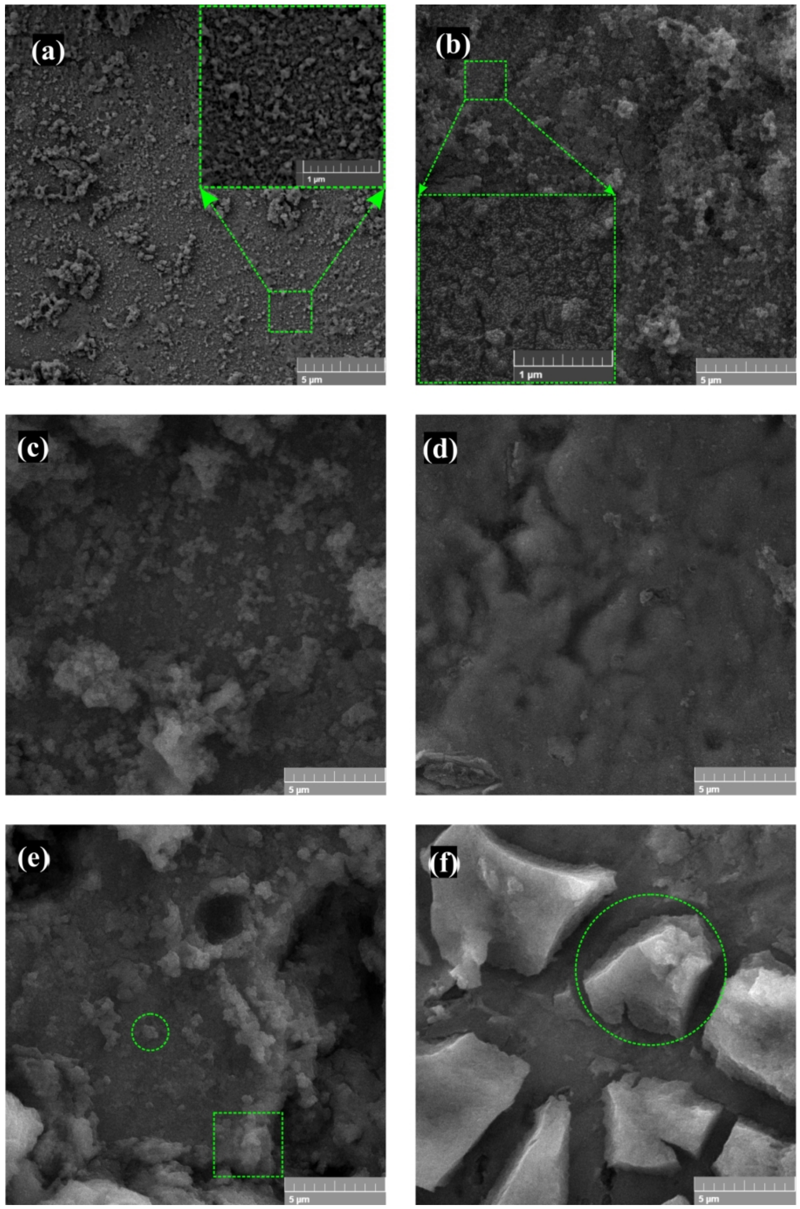

Figure 7. FE-SEM micrographs presenting the morphology of a) ACP/TiO_2 and b) ACP+ChOL/TiO_2 on Ti; ACP/TiO_2 coating on Ti immersed in SBF for c) 72 h and e) 240 h; ACP+ChOL/TiO_2 coating on Ti immersed in SBF for: d) 72 and f) 240 h.

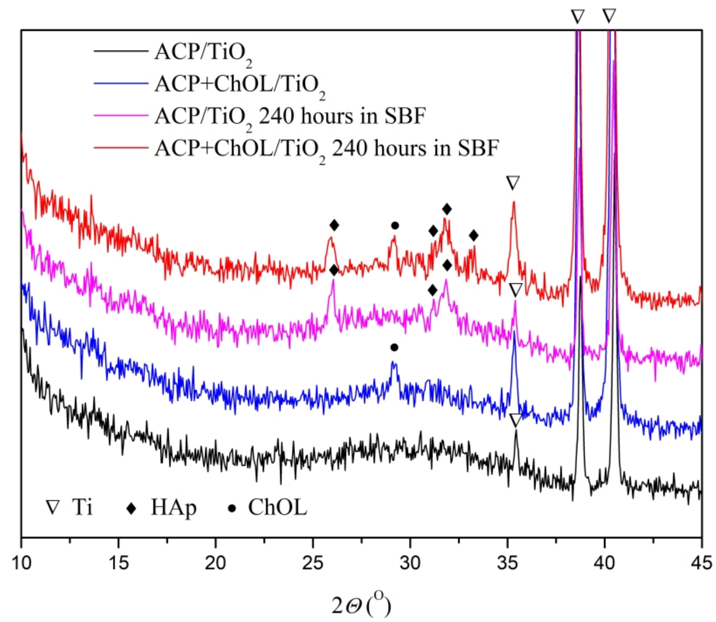

Figure 8. XRD patterns of ACP/TiO_2 and $ACP+ChOL/TiO_2$ composite coatings before and after immersion in SBF for 240 h at 37 °C.

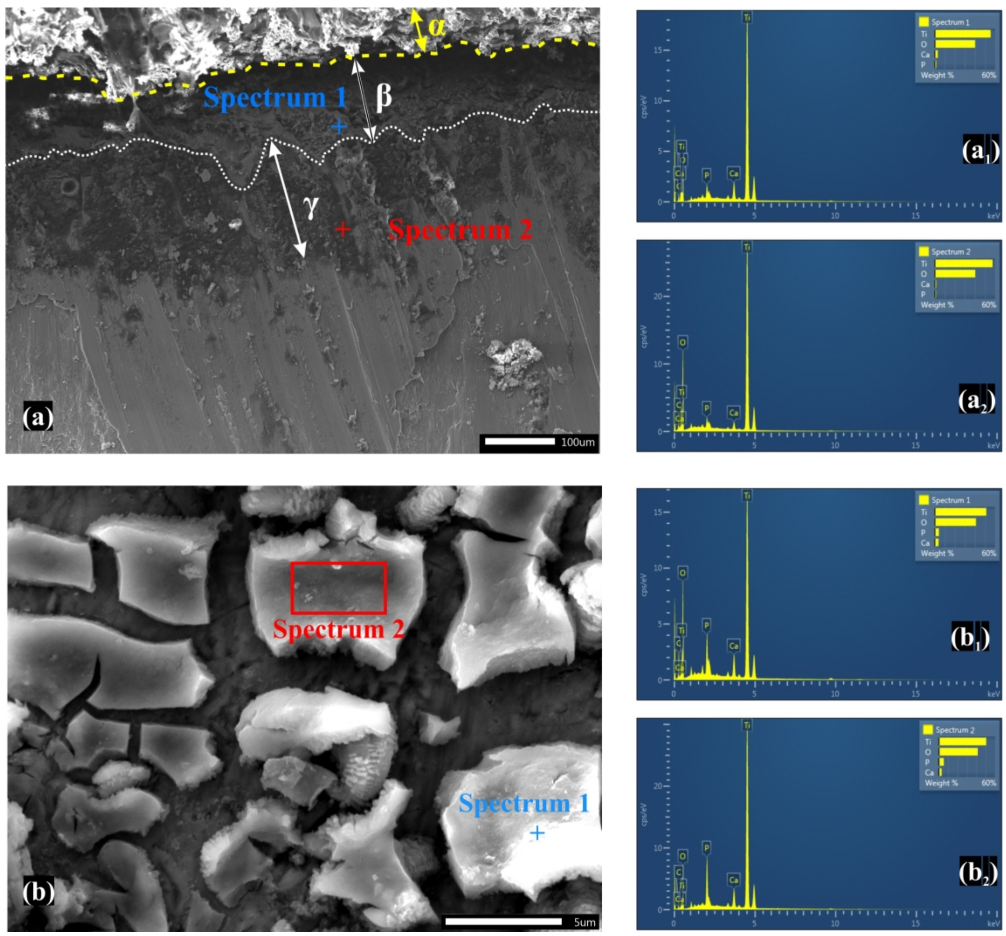

Figure 9. Analysis of sample surfaces a) SEM of cross-section of ACP+ChOL/TiO_2, a_1) EDS Spectrum 1, a_2) EDS Spectrum 2, b) SEM of ACP+ChOL/TiO_2 sample after immersion in SBF for 240 h, b_1) EDS Spectrum 1 and b_2) EDS Spectrum 2

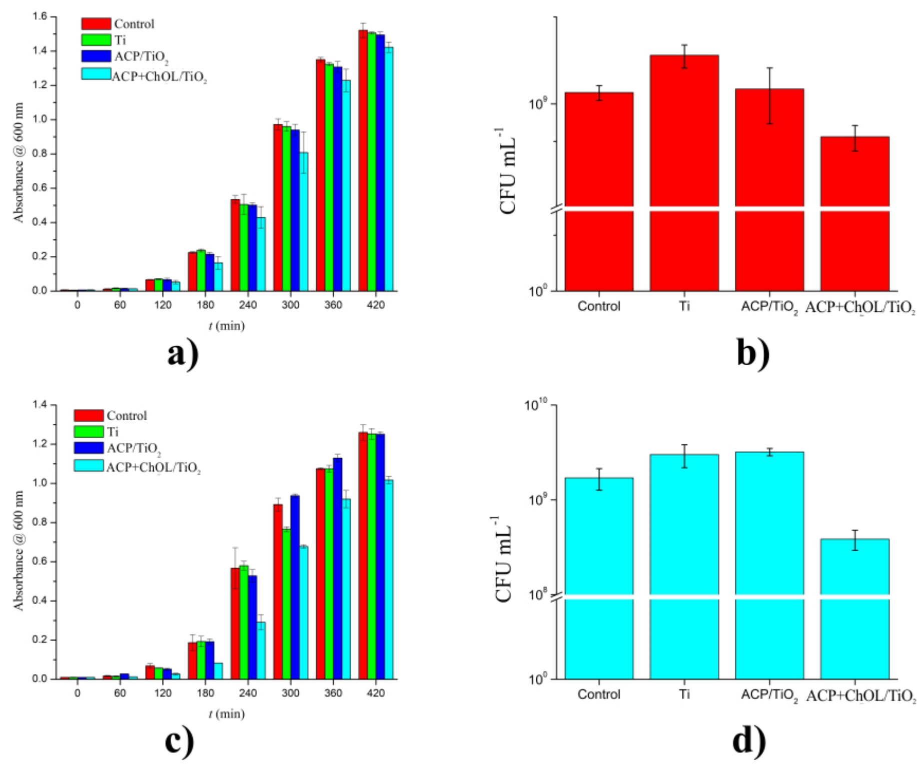

Figure 10. Growth curve measured by optical density measurements for: a) *Staphylococcus aureus* and c) *Pseudomonas aeruginosa* PAO1*. Viable cell count after 420 min for: b) *Staphylococcus aureus* and d) *Pseudomonas aeruginosa*.*Measurement at 180 min for ACP+ChOL/TiO_2 has error bar, but the error is 7×10^{-4}